



Nighttime and daytime dark oxidation chemistry in wildfire plumes: an observation and model analysis of FIREX-AQ aircraft data

Zachary C. J. Decker^{1,2,3}, Michael A. Robinson^{1,2,3}, Kelley C. Barsanti⁴, Ilann Bourgeois^{1,2}, Matthew M. Coggon^{1,2}, Joshua P. DiGangi⁵, Glenn S. Diskin⁵, Frank M. Flocke⁶, Alessandro Franchin^{1,2,6}, Carley D. Fredrickson⁷, Georgios I. Gkatzelis^{1,2,a}, Samuel R. Hall⁶, Hannah Halliday^{5,b}, Christopher D. Holmes⁸, L. Gregory Huey⁹, Young Ro Lee⁹, Jakob Lindaas¹⁰, Ann M. Middlebrook¹, Denise D. Montzka⁶, Richard Moore¹¹, J. Andrew Neuman^{1,2}, John B. Nowak¹¹, Brett B. Palm^{7,c}, Jeff Peischl^{1,2}, Felix Piel^{12,13}, Pamela S. Rickly^{1,2}, Andrew W. Rollins¹, Thomas B. Ryerson¹, Rebecca H. Schwantes^{1,2}, Kanako Sekimoto¹⁴, Lee Thornhill^{5,11}, Joel A. Thornton⁷, Geoffrey S. Tyndall⁶, Kirk Ullmann⁶, Paul Van Rooy⁴, Patrick R. Veres¹, Carsten Warneke^{1,2}, Rebecca A. Washenfelder¹, Andrew J. Weinheimer⁶, Elizabeth Wiggins^{5,15}, Edward Winstead^{5,11}, Armin Wisthaler^{12,13}, Caroline Womack^{1,2}, and Steven S. Brown^{1,3}

¹NOAA Chemical Sciences Laboratory (CSL), Boulder, CO 80305, USA

²Cooperative Institute for Research in Environmental Sciences, University of Colorado Boulder, Boulder, Co 80309, USA

³Department of Chemistry, University of Colorado Boulder, Boulder, CO 80309-0215, USA

⁴Department of Chemical and Environmental Engineering, College of Engineering – Center for Environmental Research and Technology (CE-CERT), University of California, Riverside, Riverside, CA 92507, USA

⁵NASA Langley Research Center, MS 483, Hampton, VA 23681, USA

⁶Atmospheric Chemistry Observations and Modeling Laboratory, National Center for Atmospheric Research, Boulder, CO 80301, USA

⁷Department of Atmospheric Sciences, University of Washington, Seattle, WA 98195, USA

⁸Department of Earth, Ocean, and Atmospheric Science, Florida State University, Tallahassee, FL 32304, USA

⁹School of Earth and Atmospheric Sciences, Georgia Institute of Technology, Atlanta, GA 30332, USA

¹⁰Department of Atmospheric Science, Colorado State University, Fort Collins, CO 80523, USA

¹¹Science Systems and Applications, Inc. (SSAI), Hampton, VA 23666, USA

¹²Institute for Ion Physics and Applied Physics, University of Innsbruck, 6020 Innsbruck, Austria

¹³Department of Chemistry, University of Oslo, 0315 Oslo, Norway

¹⁴Graduate School of Nanobioscience, Yokohama City University, Yokohama, Kanagawa, 236-0027, Japan

¹⁵Universities Space Research Association, Columbia, MD, USA

^anow at: Institute of Energy and Climate Research, IEK-8: Troposphere, Forschungszentrum Jülich GmbH, Jülich, Germany

^bnow at: EPA Office of Research and Development, RTP, NC 27711, USA

^cnow at: Atmospheric Chemistry Observations and Modeling Laboratory, National Center for Atmospheric Research, Boulder, CO 80301, USA

Correspondence: Steven S. Brown (steven.s.brown@noaa.gov)

Received: 26 March 2021 – Discussion started: 12 April 2021

Revised: 23 September 2021 – Accepted: 24 September 2021 – Published: 8 November 2021

Abstract. Wildfires are increasing in size across the western US, leading to increases in human smoke exposure and associated negative health impacts. The impact of biomass burning (BB) smoke, including wildfires, on regional air quality depends on emissions, transport, and chemistry, including oxidation of emitted BB volatile organic compounds (BBVOCs) by the hydroxyl radical (OH), nitrate radical (NO_3), and ozone (O_3). During the daytime, when light penetrates the plumes, BBVOCs are oxidized mainly by O_3 and OH. In contrast, at night or in optically dense plumes, BBVOCs are oxidized mainly by O_3 and NO_3 . This work focuses on the transition between daytime and nighttime oxidation, which has significant implications for the formation of secondary pollutants and loss of nitrogen oxides ($\text{NO}_x = \text{NO} + \text{NO}_2$) and has been understudied. We present wildfire plume observations made during FIREX-AQ (Fire Influence on Regional to Global Environments and Air Quality), a field campaign involving multiple aircraft, ground, satellite, and mobile platforms that took place in the United States in the summer of 2019 to study both wildfire and agricultural burning emissions and atmospheric chemistry. We use observations from two research aircraft, the NASA DC-8 and the NOAA Twin Otter, with a detailed chemical box model, including updated phenolic mechanisms, to analyze smoke sampled during midday, sunset, and nighttime. Aircraft observations suggest a range of NO_3 production rates ($0.1\text{--}1.5\text{ ppbv h}^{-1}$) in plumes transported during both midday and after dark. Modeled initial instantaneous reactivity toward BBVOCs for NO_3 , OH, and O_3 is 80.1%, 87.7%, and 99.6%, respectively. Initial NO_3 reactivity is $10\text{--}10^4$ times greater than typical values in forested or urban environments, and reactions with BBVOCs account for > 97% of NO_3 loss in sunlit plumes ($j\text{NO}_2$ up to $4 \times 10^{-3}\text{ s}^{-1}$), while conventional photochemical NO_3 loss through reaction with NO and photolysis are minor pathways. Alkenes and furans are mostly oxidized by OH and O_3 (11%–43%, 54%–88% for alkenes; 18%–55%, 39%–76%, for furans, respectively), but phenolic oxidation is split between NO_3 , O_3 , and OH (26%–52%, 22%–43%, 16%–33%, respectively). Nitrate radical oxidation accounts for 26%–52% of phenolic chemical loss in sunset plumes and in an optically thick plume. Nitrocatechol yields varied between 33% and 45%, and NO_3 chemistry in BB plumes emitted late in the day is responsible for 72%–92% (84% in an optically thick midday plume) of nitrocatechol formation and controls nitrophenolic formation overall. As a result, overnight nitrophenolic formation pathways account for $56\% \pm 2\%$ of NO_x loss by sunrise the following day. In all but one overnight plume we modeled, there was remaining NO_x (13%–57%) and BBVOCs (8%–72%) at sunrise.

1 Introduction

It is well known that biomass burning (BB), including wildfires, can have large impacts on air quality at local, regional, and global scales (Jaffe et al., 2020). The relative impact and importance of wildfire smoke on air quality in the western US is increasing with decreasing anthropogenic volatile organic compound (VOC) and nitrogen oxide ($\text{NO}_x = \text{NO} + \text{NO}_2$) emissions (Bishop and Haugen, 2018; Silvern et al., 2019; Warneke et al., 2012; Xing et al., 2015). This increase is compounded by growing wildfire emissions caused by anthropogenic influences such as human-caused climate change and past wildland management practices. Twentieth century suppression of western US wildfires has led to increased fuel loadings and thus fire potential (Higuera et al., 2015; Marlon et al., 2012; Parks et al., 2015). A warmer and drier climate in the western US resulting from human-caused climate change has exacerbated fire potential and has resulted in an increase in the frequency of large wildfires since the 1980s (Abatzoglou and Williams, 2016; Balch et al., 2017; Barbero et al., 2015; Dennison et al., 2014; Marlon et al., 2012; Westerling et al., 2006; Westerling, 2016; Williams et al., 2019).

Wildfires emit NO_x , nitrous acid (HONO), biomass burning VOCs (BBVOCs), and particulate matter (PM) that evolve chemically on a range of timescales, from seconds to weeks downwind (Akagi et al., 2011; Andreae and Merlet, 2001; Decker et al., 2019; Hatch et al., 2015, 2017, 2018; Koss et al., 2018; Palm et al., 2020). These emissions and their chemical products influence air quality through ozone (O_3) production, emitted PM, and secondary organic aerosol (SOA) formation (Brey et al., 2018; Jaffe et al., 2020; Jaffe and Wigder, 2012; Lu et al., 2016; Palm et al., 2020; Phuleria et al., 2005). However, the evolution of the smoke downwind is influenced by several variables such as fuel type, burn conditions, moisture content, nitrogen content, meteorology, and time of day.

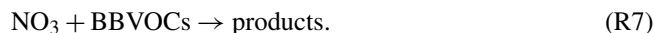
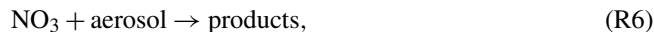
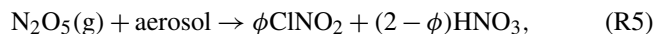
Like most atmospheric oxidation processes, the oxidation of BBVOCs is influenced by three key atmospheric oxidants: O_3 , the hydroxyl radical (OH), and the nitrate radical (NO_3). The amount of each oxidant present in a plume is influenced by emissions of NO_x , plume mixing with background air, and the amount of sunlight that penetrates a plume. Photolysis of HONO can be an important source of HO_x ($= \text{OH} + \text{HO}_2$) in the first 3 h of aging for wildfires sampled in the western US (Peng et al., 2020). Further, atmospheric background levels of O_3 , as well as photochemical O_3 production within a smoke plume, can provide O_3 for plume oxidation (Jaffe and Wigder, 2012). However, there is limited understanding of the role of NO_3 oxidation in biomass burning plumes.

During daytime, NO_3 is rapidly destroyed by photolysis (Reaction R1), and in urban plumes it is destroyed even more rapidly by reaction with NO (Reaction R2, $\tau < 10\text{ s}$) (Brown and Stutz, 2012; Wayne et al., 1991).



Therefore, although the role of NO_3 in nighttime BBVOC oxidation has been considered previously, the role of NO_3 as a daytime oxidant has been neglected (Decker et al., 2019; Keywood et al., 2015; Kodros et al., 2020; Palm et al., 2020).

Despite the potential for rapid loss of NO_3 with sunlight and NO , wildfire plumes provide a unique environment which promotes NO_3 chemistry. NO_3 is produced within a smoke plume by the gas-phase reaction of O_3 and NO_2 (Reaction R3) and is a precursor for N_2O_5 (Reaction R4), a NO_x reservoir (Brown and Stutz, 2012). N_2O_5 may undergo heterogeneous uptake to form ClNO_2 and HNO_3 according to the branching ratio ϕ (Reaction R5) (Chang et al., 2011; McDuffie et al., 2018). NO_3 can also be directly taken up by aerosol (Reaction R6) or react with BBVOCs (Reaction R7).



Modeled NO_3 reactivity was found to be mostly (> 99 %) from reactions with BBVOCs (Reaction R7) as opposed to heterogeneous reactions with aerosol particles (Reactions R5–R6) in an agricultural burning plume sampled after sunset (Decker et al., 2019). This is the result of elevated concentrations of several highly reactive BBVOCs within the plume. Specifically, directly emitted aromatic alcohols (phenolics, i.e., six-membered aromatic rings with an alcohol functional group, which are distinct from the broader class of oxygenated aromatics that also includes furans, furfals, etc.) react with NO_3 at near the gas-kinetic limit to form nitrophenolics, a subset of nitroaromatics, and secondary organic aerosol (Akherati et al., 2020; Finewax et al., 2018; Lauraguais et al., 2014; Liu et al., 2019; Xie et al., 2017). Nitrophenolics absorb strongly in the ultraviolet and visible regions of the solar spectrum and are expected to significantly contribute to brown carbon (BrC) absorption (Palm et al., 2020; Selimovic et al., 2020). Phenolic reactions with OH in the presence of NO_x also form nitrophenolics but at one-third the yield (Finewax et al., 2018).

Wildfire emissions typically peak in the midafternoon to evening and continue to emit smoke into the night (Giglio, 2007; Li et al., 2019). Furthermore, large smoke plumes can be optically thick, with little photolysis at their center. This means that most smoke plumes will be oxidized in the dark during some, if not all, of their transport. Yet, the vast majority of in situ field investigations of biomass burning smoke has been conducted under sunlight, and most analyses of daytime smoke plumes have so far focused on plume oxidation

by OH and O_3 only (Coggon et al., 2019; Keywood et al., 2015; Liu et al., 2016; Palm et al., 2020).

In the summer of 2019, both the NOAA Twin Otter and the NASA DC-8 aircraft executed a series of research flights sampling smoke plumes as part of the Fire Influence on Regional to Global Environments and Air Quality (FIREX-AQ) campaign. Here, we present a detailed analysis of smoke plumes from three fires using observations from FIREX-AQ to constrain a detailed zero-dimensional (0-D) chemical box model. We investigate one optically thick plume emitted midday, three smoke plumes emitted near or at sunset, and one theoretical plume emitted after sunset. We discuss the reactivity and competitive oxidation for all oxidants, NO_3 , O_3 , and OH , toward a suite of BBVOCs. Further, we detail the oxidation pathways of phenolics, discuss the variables that affect the yield of nitrophenolics, and describe how nitrophenolics have a significant impact on NO_x loss and fate.

2 Methods

2.1 Aircraft measurements

FIREX-AQ was a large-scale multi-platform campaign that took place during the summer of 2019 in the United States to study both wildfire and agricultural burning smoke. Both the NOAA Twin Otter and the NASA DC-8 aircraft executed a series of research flights sampling smoke plumes as part of this campaign. A main science goal of the NOAA Twin Otter was to investigate nighttime plume chemistry. However, due to a less active fire season in 2019 (NIFC, 2019) and to the decreasing smoke injection height with time of day for the sampled fires, smoke emitted after dark proved difficult to sample reliably within the altitude range of the NOAA Twin Otter. While the NOAA Twin Otter sampled over a dozen plumes after sunset, plume age estimates (described below) suggest that these plumes were emitted before or at sunset. The NASA DC-8 aircraft sampled large, optically thick, plumes both midday and near sunset. In the following sections we briefly describe the instrumentation used for this analysis, which are listed in Table S1 in the Supplement. More information and data can be found at <https://csl.noaa.gov/projects/firex-aq/twinotterCHEM/> (last access: 24 October 2021), <https://espo.nasa.gov/firex-aq> (last access: 24 October 2021), and <https://www-air.larc.nasa.gov/missions/firex-aq/index.html> (last access: 24 October 2021).

2.1.1 NOAA Twin Otter instrument descriptions

The NOAA Twin Otter sampled nine wildfires with 39 flights between 3 August and 5 September 2019 in the western US. The aircraft was based mainly in Boise, ID, and briefly in Cedar City, UT. The NOAA Twin Otter payload limited flight duration to 3.0 h or less, and the aircraft typically flew 2–3 times in a day to achieve plume sampling from midafternoon into the night. Aircraft speed was $71.8 \pm 3.8 \text{ m s}^{-1}$ (average

$\pm 1 - \sigma$), which yields a horizontal resolution of ~ 70 m for the in situ 1 s measurements. Attempts to probe the same air mass downwind, known as Lagrangian sampling, proved difficult to achieve due to complex plume structure, terrain, and airspace. Therefore, we define the sampling strategy as semi-Lagrangian. Even so, estimated emission times (calculated from estimated plume ages) suggest that smoke sampled on successive intercepts at the Castle fire and 204 Cow fire (simply referred to as Castle and Cow, respectively, from here on) plume centers was emitted within 3 and 10 min time periods, respectively. However, plume age uncertainties for the Cow plume are large (Table S2 in the Supplement).

This analysis uses NOAA Twin Otter observations of BBVOCs and HONO from a University of Washington iodide high-resolution time-of-flight chemical ionization mass spectrometer (UW I⁻ HR ToF CIMS, 2 Hz; Lee et al., 2014) as well as a Tenax cartridge sampler with subsequent GC \times GC analysis for speciated BBVOCs (intermittent transect integrations; Hatch et al., 2015; Mondello et al., 2008), which we use to support mass assignments from the UW I⁻ HR ToF CIMS for some phenolic compounds (see the Supplement).

We use data from a commercial cavity ring-down spectrometer (Picarro G2401m) for measurements of CO, CO₂, and CH₄ (0.5 Hz; Crosson, 2008). We use measurements from a custom chemiluminescence instrument (CL, 1 Hz) for NO, NO₂, and O₃ (Sparks et al., 2019). Aerosol surface area measurements were collected by an ultrahigh-sensitivity aerosol spectrometer (UHSAS, 1 Hz; Kupc et al., 2018). The UHSAS data were corrected for coincidence up to a factor to 1.4, following the method described in Kupc et al. (2018). The sample for the UHSAS was diluted up to a factor of 2.9 for part of the flights to increase accuracy at higher concentrations. The aircraft had a standard meteorological probe (Aventech ARIM 200) for temperature, pressure, relative humidity, wind speed, and direction. We use NO₂ photolysis rates (j_{NO_2}) collected by upward- and downward-facing j_{NO_2} filter radiometers (Metcon GmbH, 1 Hz; Kupc et al., 2018; Warneke et al., 2016).

2.1.2 NASA DC-8 instrument descriptions

The NASA DC-8 aircraft sampled 14 wildfires in the western US while based in Boise, ID, as well as about 90 prescribed agricultural southeastern US fires while based in Salina, KS, between 22 July and 5 September 2019. Aircraft speed was $167.2 \pm 3.4 \text{ m s}^{-1}$, which yields a horizontal resolution of ~ 167 m for the in situ 1 s measurements. Similar to the NOAA Twin Otter, sampling was semi-Lagrangian. However, smoke emission times for the plume centers of Williams Flats fires 1 and 2 (referred to as WF1 and WF2 from here on) covered a larger time period (~ 30 – 60 min) compared to the NOAA Twin Otter (Table S2 in the Supplement).

In this analysis we use measurements of CO from a tunable diode laser spectrometer (1 Hz; Sachse et al., 1991) when available and from a cavity enhanced spectrometer

(CES, 1 Hz; Eilerman et al., 2016) when unavailable. In the fires investigated here, both instruments agree well within $< 1\%$. Measurements of NO₂, NO_y, and O₃ are provided by a NOAA chemiluminescence (1 Hz; Pollack et al., 2010; Ridley et al., 1992; Stedman et al., 1972) instrument. When measurements of NO₂ by the NOAA CL instrument are unavailable, we use measurements by a NOAA CES (1 Hz; Min et al., 2016). These two measurement methods of NO₂ agree within 12% for the fires we investigate. We use measurements of NO by a laser-induced fluorescence instrument (1 Hz; Rollins et al., 2020). Measurements of BBVOCs and HONO are taken from the NOAA I⁻ ToF CIMS (1 Hz; Neuman et al., 2016; Veres et al., 2020) as well as the University of Innsbruck proton transfer reaction time-of-flight mass spectrometer (UIBK PTR ToF MS; Müller et al., 2014). Peroxyacetyl nitrate measurements were performed by a thermal dissociation CIMS (1 Hz, Ro Lee et al., 2020). Aerosol surface area measurements are taken from a scanning mobility particle sizer and laser aerosol spectrometer (SMPS and LAS, 1 Hz, LAS, 2021; Moore et al., 2021; SMPS, 2021). Spectrally resolved actinic flux was measured with separate upward- and downward-facing actinic flux optics (CAFS, 1 Hz; Shetter and Müller, 1999). These fluxes were used to calculate photolysis rates using the photochemistry routine contained in the NCAR TUV model (v5.3.2, <https://www2.acom.ucar.edu/modeling/tropospheric-ultraviolet-and-visible-tuv-radiation-model>, last access: 24 October 2021).

2.1.3 Plume age determination

Plume age estimates are made by air parcel trajectories computed in the HYSPLIT (HYbrid Single-Particle Lagrangian Integrated Trajectory) model with multiple high-resolution meteorological datasets (HRRR 3 km, NAM CONUS nest 3 km, and GFS 0.25°). These estimates account for buoyant plume rise as well as horizontal advection. Uncertainties in plume age are determined from spread between the meteorological datasets, mismatch between observed and archived winds, and trajectory spatial error in missing the known fire source. Typical uncertainties are 25% of the estimated age (Holmes et al., 2020).

2.2 Fire descriptions

This analysis focuses on four semi-Lagrangian experiments from three separate fire complexes: the Castle fire plume in northern Arizona, the 204 Cow fire plume in central Oregon, and two from the Williams Flats fire plume in eastern Washington. Table 1 summarizes fire locations, sampling platform, sampling times, and fuel types (Inciweb, 2019a, b, c). Figure 1 displays flight paths. We select the above plume samplings among others because of their data coverage, potential for active chemistry, and sunset-like conditions defined as the following: (1) sampled by semi-Lagrangian transects

Table 1. Details of fires studied.

Fire name	County/state	Latitude	Longitude	Date sampled	Time sampled	Aircraft	Fuel
Williams Flats	Ferry/Washington	47.9392	−118.6183	7 Aug	16:30–17:45 PDT & 18:00–19:30 PDT	DC-8	Short grass, ponderosa timber
Castle	Coconino/Arizona	36.5312	−112.2281	21 Aug	18:00–19:15 MST	Twin Otter	Mixed conifer
204 Cow	Grant/Oregon	44.2851	−118.4598	28 Aug	20:00–22:00 PDT	Twin Otter	Primarily lodgepole pine with conifer

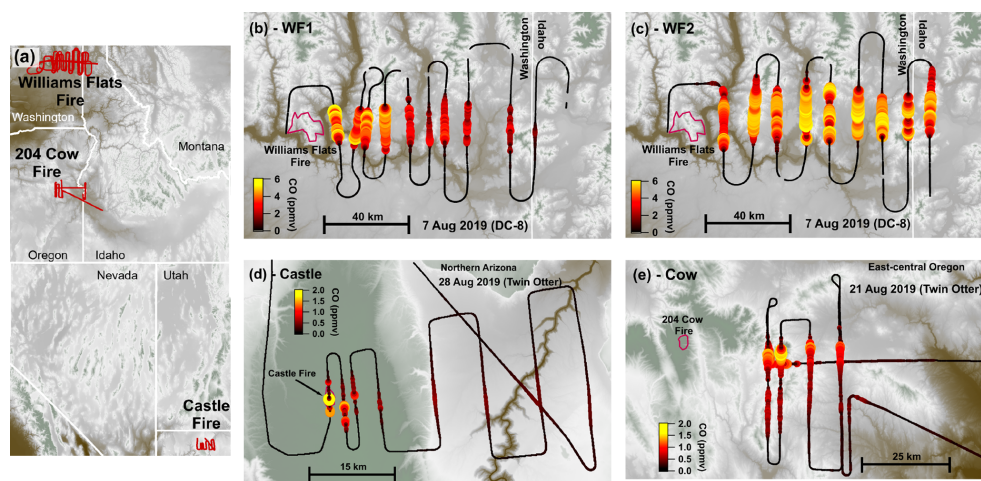


Figure 1. Flight maps colored by elevation. Overview map (a) showing flight tracks (red) with detailed flight maps of the WF1 transects (b), WF2 transects (c), Castle transects (d), and 204 Cow transects (e). Panels (b)–(e) are colored and sized by CO. Fire boundaries are approximate and indicated by red outlines. The flight path is shown in black and sized by CO.

roughly perpendicular to the prevailing wind direction; (2) had available measurements of CO, NO_x, HONO, O₃, photolysis rates, and aerosol surface area; (3) contained either reduced plume-center photolysis ($j\text{NO}_2 < 10^{-3} \text{ s}^{-1}$) or plume ages < 3 h by sunset; and (4) sampled a plume age range > 1 h.

The WF fire started on 2 August 2019 and grew to a total of 179.9 km² before it was contained on 25 August 2019. The fuel was mostly short grass (~0.3 m tall) as well as ponderosa and mixed conifer timber (Inciweb, 2019c). The DC-8 aircraft performed three semi-Lagrangian smoke transect patterns on 7 August 2019 when the fire had burned about 101.2 km². This study focuses on the first two sampling patterns: the WF1 (Fig. 1b) and WF2 (Fig. 1c). WF1 contained smoke emitted from about 14:00–16:00 PDT (local time) or the early to late afternoon, while the second pattern sampled smoke emitted near sunset. The sampled smoke varied in age from 36 min–4 h.

The Castle fire began on 12 July 2019 and was allowed to burn the mixed conifer fuel in a defined area that eventually reached 78.4 km², and it burned out on 15 October 2019 (Inciweb, 2019b). The Twin Otter aircraft performed one semi-Lagrangian transect pattern during sunset on 21 August 2019 when small pockets of remaining fuel types were burning

(Fig. 1d). The sampled smoke varied in age from approximately 2 min–1.5 h. The Castle fire had a neighboring fire named Ikes. Smoke from the Ikes fire visually mixed (Fig. S1 in the Supplement) with the Castle fire plume after the fourth transect downwind of the Castle fire (Fig. 1d). For that reason, this analysis focuses on the first four transects only.

The Cow fire started on 9 August 2019 and was allowed to burn eventually reaching 39.1 km² by 15 September 2019. The fuel was mainly lodgepole pine at lower elevations and mixed conifer at higher elevations with abundant downed timber. The Twin Otter aircraft performed three semi-Lagrangian transect patterns on 28 August 2019, by which time the fire had burned 13.9 km² (Inciweb, 2019a). This study focuses on the third semi-Lagrangian transect pattern, which was conducted after sunset (Fig. 1e). The sampled smoke in this analysis had aged approximately 2–3 h.

2.3 Box model description

We modeled smoke plumes from three fires (Castle, Cow, and WF). We present four model cases (Castle, Cow, WF1, WF2) constrained by aircraft observations and one case (denoted Dark) identical to the WF2 case except all modeled photolysis frequencies are set to zero. We consider the Dark

model run only for the WF2 case and not the others since it is a hypothetical exercise intended to illustrate the evolution of smoke emitted after dark, a case for which there were no available observations from the 2019 campaign. The Dark case is used to understand the effect of photolysis on the WF2 model run.

There were sufficient emissions for the WF1, WF2, Dark, and Cow model runs such that there were emissions remaining above background levels after 12 h of model time. The Cow, WF2, and Dark cases are run from emission until sunrise the following day (about 12 h). The Castle case is run for 2.6 h until all BB emissions are near ($\ll 1\%$) background levels. We run the WF1 case until the age of the oldest sampled smoke (~ 4 h), because we do not have any observations of photolysis rates with which to constrain the model past that point.

Box modeling was performed using the Framework for 0-D Atmospheric Modeling (F0AM) (Wolfe et al., 2016) with chemistry and emissions described in the following section. We start the model at the emission time (age = 0) of the earliest smoke transect (the youngest sampled smoke), which occurred between 2 min and 2 h before the first plume transect, depending on the plume. In most cases, we use an iterative method constrained to a subset of observations (described in Sect. 2.3.3) to estimate emissions.

While all plumes were sampled by aircraft following a semi-Lagrangian strategy, we model each plume as if it were Lagrangian – i.e., it is assumed that the emissions and fire conditions were constant over the course of sampling. Further, we constrain our model to plume-center observations, because we model only the plume center and represent mixing through a dilution term. Consequently, the model does not represent differences in chemical regimes that may occur between the center and edge of a plume. Components of our model have been used for other applications (Decker et al., 2019; McDuffie et al., 2018; Robinson et al., 2021; Wagner et al., 2013). However, the combination of the components is specific to only this work.

2.3.1 Chemistry and emissions

Our model uses the Master Chemical Mechanism (MCM, v3.3.1 via <http://mcm.york.ac.uk>, last access: 23 September 2021), in conjunction with a NOAA biomass burning mechanism included in F0AM v4.0 (Bloss et al., 2005; Coggon et al., 2019; Decker et al., 2019; Jenkin et al., 1997, 2003, 2012, 2015) and updates to OH- and NO₃-initiated oxidation of phenolic compounds (Bolzacchini et al., 2001; Calvert et al., 2011; Finewax et al., 2018; Nakao et al., 2011; Olariu et al., 2002, 2013; Schwantes et al., 2017). Briefly, we update the phenolic oxidation product yields of catechol, methylcatechol, and three dimethylcatechols reacting with NO₃ and OH. Further, we expand the phenolic oxidation pathways in the MCM from 50 to 140 reactions by extrapolating anal-

ogous branching ratios, rate coefficients and products from studies of phenol and cresol oxidation (see the Supplement).

We initiate the model, as discussed in Sect. 2.3.3, using an emissions inventory of 302 BBVOCs in the form of emission ratios (ERs).

$$ER_x = \frac{X \text{ (ppbv)}}{CO \text{ (ppmv)}}, \quad (1)$$

Note that an ER is used to describe an emission (when smoke age = 0) and is different than a normalized excess mixing ratio (defined in Sect. 2.4.1) used to describe observations when smoke age > 0. The ER inventory is described in detail in Decker et al. (2019) and uses an average of BBVOC emission ratios of ponderosa pine fuel from the Fire Lab at Missoula Experiment (FLAME-4) (Hatch et al., 2017) and the Fire Influence on Regional and Global Environments Experiment (FIREX lab) (Koss et al., 2018) with rate coefficients taken from literature when available or estimated when unavailable. Approximately 250 BBVOCs in the inventory are not included in the MCM and do not have published mechanisms. Therefore, reactions of those compounds with NO₃, OH, and O₃ lead to a generic product.

The model includes heterogeneous NO₃ and N₂O₅ uptake onto aerosol, calculated for NO₃ heterogeneous reactivity, as

$$k_{NO_3}^{\text{aerosol}} = K_{\text{eq}}[NO_2]k_{N_2O_5} + k_{NO_3+\text{aerosol}}, \quad (2)$$

where $k_{NO_3}^{\text{aerosol}}$ is a first-order rate coefficient, K_{eq} is the equilibrium rate constant for Reaction (R4), and $k_{NO_3+\text{aerosol}}$ is a first-order rate coefficient for uptake expressed below. Note, however, that the following equation applies for small uptake coefficients and small aerosol diameters where gas-phase diffusion does not limit uptake. For large particle diameters or large uptake coefficients, the simplified heterogeneous uptake equation requires a correction for gas-phase diffusion (Fuchs and Sutugin, 1970; Kolb et al., 2010). For accumulation mode particles on the order of 100 nm and uptake coefficients on the order of 0.01, this correction is not important.

$$k_{x+\text{aerosol}} = \frac{\gamma \bar{c} SA}{4} \quad (3)$$

Here γ is the aerosol uptake coefficient, \bar{c} is the mean molecular speed, and SA is the measured aerosol surface area at plume center. We use $\gamma_{N_2O_5} = 10^{-2}$ and $\gamma_{NO_3} = 10^{-3}$ (McDuffie et al., 2018).

2.3.2 Model constraints

Our model is constrained to plume-center and background measurements of aerosol surface area, photolysis rates, O₃, CO, NO_x, HONO, and total oxidized nitrogen (NO_y). Measurements of NO_y are only available from the DC-8 measurements. We also constrain our models to the meteorological conditions pressure, temperature, and relative humidity. Fire emissions and photolysis conditions can change rapidly;

therefore, we constrain the model to a subset of plume transects. We chose transects that showed a monotonic decrease in CO with distance from the fire, cover an age range of at least 1 h, and have similar emission times as shown in Figs. S2–S3 and Table S2.

All model runs included a constant first-order plume dilution rate coefficient (k_{dil}) determined by applying an exponential fit to observed CO as a function of plume age (Fig. S3 in the Supplement). We fit only points used to constrain the model and fixed the exponential fit offset to the observed CO background. We applied k_{dil} to all species in the model. We find values of k_{dil} that range between $1.6\text{--}46 \times 10^{-5} \text{ s}^{-1}$ (Table S3 in the Supplement), equivalent to a lifetime ($\tau_{\text{dil}} = 1/k_{\text{dil}}$) of 0.6–17.3 h.

Plume-center observations were determined using a “top 5 %” method as described by Peng et al. (2020). Briefly, within a transect we determine the location of the greatest 5 % of observations for CO and use that location of the plume for analysis of other compounds. This method obtains an average observation for the center, or most concentrated, parts of the plume. Reported uncertainties are the $1 - \sigma$ variability of the top 5 % region and instrument uncertainties added in quadrature.

Particulate matter in BB plumes attenuates sunlight, thus photolysis rates, in a process we refer to as plume darkening. In WF plumes we use plume-center observations of 20 photolysis rates (listed in Table S4 in the Supplement), but for the Castle and Cow plumes only $j\text{NO}_2$ is available due to the limited instrument payload on the NOAA Twin Otter. Average attenuation of $j\text{NO}_2$ within the WF1 and WF2 plumes was 96 % (meaning $j\text{NO}_2$ at plume center was 4 % of $j\text{NO}_2$ outside of the plume). Plume-center attenuation of $j\text{NO}_2$ was 29 % for the Castle plume. We sample the Cow plume after sunset and therefore do not have observation of $j\text{NO}_2$ while the smoke was under sunlight (0–2 h). We estimate that plume-center $j\text{NO}_2$ attenuation was 34 %. This estimate was made by comparing $j\text{NO}_2$ attenuation to plume size (by CO) in the WF and Castle model runs and is consistent with $j\text{NO}_2$ attenuation in plumes emitted from the Cow fire sampled on other days. All other photolysis rates were estimated using a ratio of the observed $j\text{NO}_2$ to calculated photolysis rates using an MCM trigonometric solar zenith angle (SZA) function below.

$$J = l \cdot \cos(\text{SZA})^m \cdot e^{-n \cdot \sec(\text{SZA})}, \quad (4)$$

where l , m , and n are derived from least squares fits to j values from a radiative transfer model and literature cross sections and quantum yields. This calculation is a standard photolysis value method in F0AM and is described by Jenkin et al. (1997). However, this method does not account for overhead O_3 column, surface albedo, aerosol, or other effects.

In all of the plumes studied here, observed $j\text{NO}_2$ rates are below 10^{-3} s^{-1} excluding the first few minutes of the Castle plume (see Fig. 2). Values of $j\text{NO}_2$ in the WF2 plume remained low, near 10^{-4} s^{-1} during the sampling time. In con-

trast, the WF1 plume exhibits increasing $j\text{NO}_2$ rates, which eventually reach $8 \times 10^{-4} \text{ s}^{-1}$. Differences in the photolysis rates between the first and second pass are likely due to the setting sun. Finally, observations of photolysis rates are negligible in the Cow plume as it was sampled after sunset.

2.3.3 Model initiation

In all plumes except the Castle plume, our first transect sampled smoke 36 min–2 h old; therefore, we implemented an iterative method (McDuffie et al., 2018; Wagner et al., 2013) to estimate initial emissions (at age = 0). We began with best-guess estimates of CO, NO, NO_2 , HONO, O_3 , and all BB-VOCs (determined by CO and our emissions inventory by Eq. 1) and then systematically changed these initial conditions to minimize the differences between model output and observations downwind. Initial conditions in the Castle run were taken directly from observations of NO, NO_2 , O_3 , CO, HONO, phenol, catechol, cresol, and methylcatechol in the first transect where the plume age was 3 ± 1 min and therefore was close to age = 0. We initiated the remaining 298 BBVOCs by using CO and Eq. (1). Initial conditions for all cases are shown in Table S5 in the Supplement. In all cases, backgrounds of NO, NO_2 , O_3 , CO, and HONO were taken as an average outside of the plume, and BBVOC backgrounds were assumed to be zero. Background mixing ratios used in all cases are shown in Table S3.

We determined best-guess estimates of CO and HONO directly from observations of the first transect. To determine a best-guess estimate for NO_x , we used the sum of observed NO and NO_2 for the Cow run or NO_y minus HONO (as NO_y will contain HONO) for the WF runs. Best-guess estimates of O_3 were determined using an average of background O_3 observations from a flight leg upwind of the fire and outside of the plume transects, which can vary (Table S6 in the Supplement).

We began iteration with CO and k_{dil} by increasing best-guess estimates of CO and varying k_{dil} within the fit errors until we minimized the differences between observed and modeled CO. This, in turn, determines the emissions of BB-VOCs by Eq. (1). Next, we iterated NO_x , HONO, and the NO/ NO_x ratio such that the sum of NO_x and HONO did not exceed the observed NO_y , and the initial NO/ NO_x ratio remained between 0.6–1 (Roberts et al., 2020). Lastly, we iterated the initial and background O_3 . As explained in Sect. 2.4, we were required to iterate on background O_3 in some model runs in order to achieve agreement between model and observations. We repeated the above process to minimize the differences between model and observations. In an attempt to avoid finding a local solution, as opposed to the “best” solution, we reversed the order of iterating O_3 , NO_x , and HONO when repeating the above process.

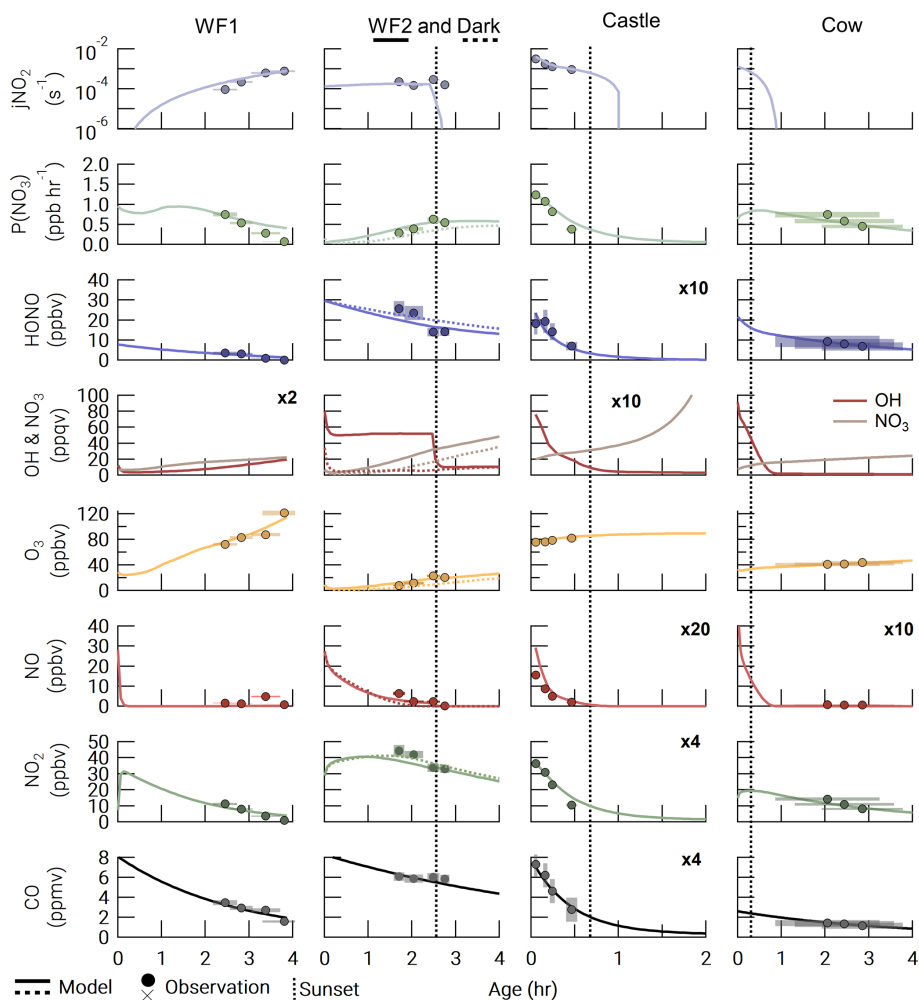


Figure 2. Observations (closed circles) and model output (lines) for all model runs. The Dark run is shown as a dashed line in the WF2 column. The time of sunset (defined as when the solar zenith angle reaches 90°) is indicated by a vertical dashed line. Observation errors (y error: variability in the observation at plume center and instrument uncertainty added in quadrature; x error: uncertainty in plume age determination) are shown as shaded xy boxes.

2.4 Observations and model comparison

Accurately modeling the first-order loss of CO is critical as it determines the overall plume dilution rate coefficient and initial BBVOC mixing ratios. Median differences in modeled and observed CO range from 39.7–307.4 ppbv with a median difference of 2.8%–11.7% across all model runs. Percentage and absolute differences between the model runs and observations are detailed in Table S7 in the Supplement and Fig. 2. Median differences of NO_2 and HONO are 5.1%–32.2% and 6.6%–53.3%, respectively. There are greater percentage differences in NO_2 and HONO that arise due to lower mixing ratio observations mostly in the WF1 and Castle plumes, with a range of absolute median differences of NO_2 and HONO between 0.4–2.0 ppbv and 0.3–3.4 ppbv, respectively.

Ozone median differences vary from 0.3–6.3 ppbv with a median difference of 0.8%–27.2% across all runs. For the

WF1 and WF2 plumes, we found that a significant increase (38.5 ± 0.4 and 35.3 ± 7.5 ppbv, Tables S3 and S6) in model background O_3 compared to the upwind leg was required to capture the observed plume-center O_3 . This is due to photochemical O_3 production at the plume edges, where O_3 was as much as a factor of ~ 2 greater than the background O_3 . The increased plume edge O_3 is not captured in our plume-center model and thus requires an increase in model background O_3 .

Additional model and observation comparisons of BBVOCs, including phenolics (discussed in detail below), are included in Figs. S5–S12 in the Supplement. In most cases, the comparisons show that the model and observations agree within a factor of ~ 2 if not within observation errors.

2.4.1 Comparisons of constrained compounds

The WF fire emissions were significantly greater than the Castle and Cow fire emissions as is seen in the observed CO data (Fig. 2). Initial plume-center CO was 8.26 and 8.33 ppmv in WF1 and WF2, respectively, but 2.62 and 1.95 ppmv for Cow and Castle, respectively.

We report our observations for each species (X) relative to CO in the form of normalized excess missing ratios (NEMRs) following Yokelson et al. (2013) and shown in Fig. S4.

$$\text{NEMR} = \frac{X_{\text{Plume}} - X_{\text{Background}} (\text{ppbv})}{\text{CO}_{\text{Plume}} - \text{CO}_{\text{Background}} (\text{ppmv})} \quad (5)$$

Ozone depression and negative NEMRs at the plume center were observed in all of the sunset, nighttime, or darkened fire plumes analyzed here. Observations of $\Delta\text{O}_3/\Delta\text{CO}$ (where Δ indicates background-corrected) in the Castle plume remains at just below background levels of O_3 in all observations likely due to the small plume size and large O_3 background (82.5 ± 2.1 ppbv). Generally, $\Delta\text{O}_3/\Delta\text{CO}$ increases with plume age due to photochemical O_3 production and mixing with background O_3 . Ozone in the midday WF1 plume reaches 44.8 ± 3.4 ppbv ppmv⁻¹ of CO or 67.4 ppbv above background after 3.8 ± 0.5 h of transport.

Referring to Fig. S4, we find that observed $\Delta\text{NO}/\Delta\text{CO}$, $\Delta\text{NO}_2/\Delta\text{CO}$, and $\Delta\text{HONO}/\Delta\text{CO}$ have variable trends in all plumes. Observations of $\Delta\text{NO}/\Delta\text{CO}$ are near-zero (≤ 0.1 ppbv ppmv⁻¹) in the Castle and WF1 plumes and elevated in the WF2 and Cow plumes (0.21 ± 0.02 – 1.21 ± 0.13 ppbv ppmv⁻¹). Observed $\Delta\text{NO}/\Delta\text{CO}$ in the WF2 plume changes sharply between the first four and last five transects, suggesting changes in fire emissions or photolysis near emission. In order to avoid these changes, we use only observations from the latter to constrain our model, as discussed in Sect. 2.3.2.

There is a general decrease in $\Delta\text{NO}_2/\Delta\text{CO}$ and $\Delta\text{HONO}/\Delta\text{CO}$ over 4 h of aging. Observations of $\Delta\text{NO}_2/\Delta\text{CO}$ in the WF1 plume decrease at a faster rate than those in the WF2 plume; however, both plumes exhibit about 8.6 ppbv ppmv⁻¹ in the youngest smoke (35 ± 8 min old).

2.4.2 Comparisons of $P(\text{NO}_3)$

Emissions of NO_x from biomass burning plumes provide a source of NO_3 that is suggested to be a major oxidant for BBVOCs (Kodros et al., 2020). The instantaneous NO_3 production rate, $P(\text{NO}_3)$, is a common metric of the potential for NO_3 chemistry (Brown and Stutz, 2012).

$$P(\text{NO}_3) = k_{\text{NO}_3}[\text{NO}_2][\text{O}_3] \quad (6)$$

At the center of the plumes presented in this study, NO_3 production rates were between 0.1 and 1.5 ppbv h⁻¹ as seen in

Fig. 2. These NO_3 production rates are consistent with those found in a nighttime agricultural smoke plume measured above a rural area at the border of Missouri and Tennessee during the Southeast Nexus campaign (SENEC), which varied between 0.2 and 1.2 ppbv h⁻¹ (Decker et al., 2019). These values of $P(\text{NO}_3)$ are also similar to those found in urban plumes and forested areas. Production rates of NO_3 in urban plumes typically range within 0 – 3 ppbv h⁻¹ at night but can be larger. In forested regions, $P(\text{NO}_3)$ is typically below 1 ppbv h⁻¹ at night (Brown and Stutz, 2012).

Agreement between the modeled $P(\text{NO}_3)$ and observed $P(\text{NO}_3)$ reflects agreement between observed and modeled NO_2 and O_3 . The WF1 model run slightly overpredicts NO_2 after 3 h of aging and therefore overpredicts $P(\text{NO}_3)$. Similarly, the Cow model run slightly underpredicts NO_2 compared to observations; therefore, the trend in $P(\text{NO}_3)$ is slightly underpredicted.

2.4.3 Comparison of phenolics

Our work focuses on the role of phenolics in BB plumes and includes updated and expanded phenolic oxidation mechanisms as described in the “Expansion of Phenolic Mechanism Description” section in the Supplement. Therefore, capturing the phenolic evolution in our models is critical to understanding the importance of phenolics in BB. In the Castle case, which is initiated with observations of phenolics, we find excellent agreement for catechol, methylcatechol, phenol, and cresol (Figs. S5 and S9). Further, we find that the model run lies on the upper edges of nitrocatechol errors and the lower edge of nitrophenol errors. The model run underpredicts nitrocresol by a factor of 60. Note that we do not have available calibrations for nitromethylcatechol but do provide observations in arbitrary units for the purpose of comparing the time evolution of this compound.

Overall the model recreates the relative time evolution of nitrophenolics well. Disagreement between the model and observed compounds could be caused by many factors including, but not limited to, interfering isomers measured by the UW I⁻ HR ToF CIMS or the NOAA I⁻ ToF CIMS, variable fire ERs, and loss or production of nitrophenolics not captured by our mechanism. The MCM includes several gas-phase loss processes of nitrophenolics but no gas to particle partitioning. Nitrophenolics readily partition to the aerosol phase (Finewax et al., 2018). Further, the MCM does not include photolytic loss of nitrophenolics, despite some evidence to the contrary (Sangwan and Zhu, 2016, 2018). Omitting the aerosol loss pathway may be the cause for these discrepancies. However, precisely how these differences affect the model and observation comparison is uncertain. Therefore, when analyzing gas-phase nitrophenolic evolution, we only consider integrated formation, as discussed in Sect. 3.3.2.

All other model runs were not initiated to observations of phenolics due to the older age of smoke during the first

transect. Even so, in the Cow model run (Figs. S6 and S10) we find agreement with catechol and methylcatechol within observation errors. Modeled phenol is about a factor of 3 (Δ 1.4–2.0 ppbv) greater than the observations. Modeled cresol is about a factor of 10 greater than observations, while its oxidation product, nitrocresol, is 7 times less than the observations. Models are thus able to reproduce some, but not all, phenolic observations in the Cow plume.

Observations of phenolics in the WF plumes are limited to uncalibrated catechol and nitrocatechol observations from the NOAA I⁻ ToF CIMS (Figs. S7–S8 and S11–S12). In the WF1 model run, catechol and nitrocatechol appear to deplete faster than the model would suggest. The time evolution of nitrocatechol in the WF2 plume agrees well with the model, and in the WF1 model run the model matches the rough timing of the observed maximum signal.

3 Results and discussion

3.1 Reactivity

Instantaneous reactivity, Eq. (7) referred to simply as reactivity from here on, is used as a simplified metric to predict the competition of reactions between oxidant and BBVOC

$$k_X = \sum_i k_{X+BBVOC_i} [BBVOC_i], \quad (7)$$

where $k_{X+BBVOC}$ is a bimolecular rate coefficient for the reaction of $X + BBVOC$ (where X is O_3 , NO_3 , or OH), and k_X is an instantaneous first-order rate coefficient. Here, we calculate and detail the reactivity for O_3 , NO_3 and OH oxidation of BBVOCs to understand their predicted competition. We also discuss how reactivity of the BB plumes studied here compare to other environments.

At emission, BBVOCs account for the majority of total reactivity for OH (87.7 %), NO_3 (80.1 %), and O_3 (99.6 %) as seen by the bars in Fig. 3. HCHO and CO account for 5.1 % and 5.3 % of OH reactivity, respectively, while NO_2 accounts for a small (0.3 %) fraction. In this analysis we do not specify an aldehyde group and therefore separate HCHO from the general BBVOC groupings. We exclude O_3 reactivity to NO in Fig. 3, because during the daytime this reaction is in a rapid cycle with NO_2 photolysis and regeneration of O_3 in which odd oxygen, $O_x = NO_2 + O_3$, is conserved. Further reactions of O_3 and NO_2 can lead to loss of O_x . This analysis includes BBVOC oxidation by O_3 but not a detailed budget for O_x .

Underneath each reactivity bar in Fig. 3, we show the partitioning of the initial BBVOC reactivity. Almost three-quarters of OH reactivity is from alkenes (33.0 %), furans (25.0 %) and phenolics (16.4 %). The reactivity of NO_3 , by contrast, is controlled by phenolics (64.4 %), and O_3 reactivity is controlled by alkenes (53.8 %) and terpenes (39.2 %). Nitrate radical reactivity toward a smaller fraction of VOCs

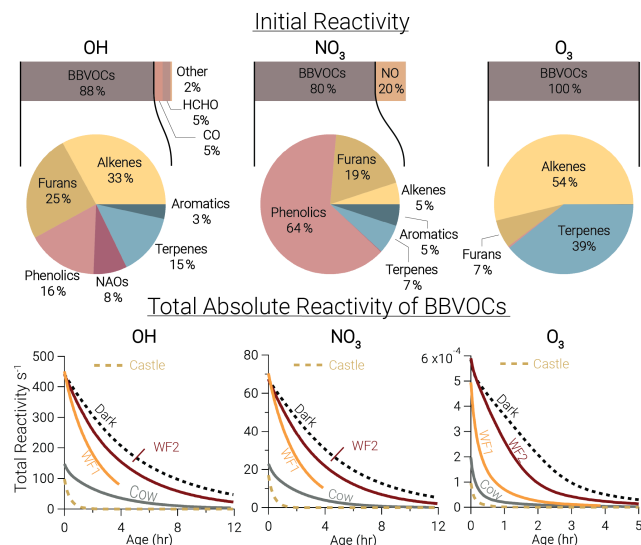


Figure 3. Bars: average (of all five model runs) initial relative instantaneous reactivity for all compounds in our model, showing that initial reactivity of BBVOCs outweighs all other compounds for all oxidants. Pie charts: initial relative reactivity of BBVOCs, showing that OH reactivity is controlled by many BBVOC groups, NO_3 reactivity by phenolics, and O_3 reactivity by alkenes and terpenes. Time series: absolute reactivity of for all model runs, showing that reactivity decays at different rates for each model run and that OH and NO_3 reactivity decay is similar.

is consistent with other reactivity analyses of OH , NO_3 , and O_3 in forest air (Palm et al., 2017).

Below each pie chart in Fig. 3, we show reactivity for OH , NO_3 , and O_3 toward BBVOCs on an absolute scale. As BBVOCs are oxidized and the plume dilutes, the plume reactivity is reduced. Decay of OH and NO_3 reactivity is nearly identical, while that of O_3 is different (e.g., WF2 and Dark). As a result, fewer BBVOCs, specifically alkenes, are oxidized in the Dark model run, keeping reactivity greater when compared to the WF2 model run.

Total initial OH reactivity toward BBVOCs ranges from $98.3\text{--}450.0\text{ s}^{-1}$. Since the modeled total reactivity is proportional to the plume's initial emission of CO, the largest plumes, WF and Dark, have the greatest total initial total reactivity. Typical OH reactivities range between $7\text{--}130\text{ s}^{-1}$ for urban plumes or $1\text{--}70\text{ s}^{-1}$ in forests (Yang et al., 2016), demonstrating that wildfire plumes can be similar to urban plumes or significantly more reactive.

Total initial O_3 reactivity toward BBVOCs ranges between 1×10^{-4} and $6 \times 10^{-4}\text{ s}^{-1}$. A recent study of a suburban site in China found O_3 reactivities toward non-methane VOCs between $2.5 \times 10^{-7}\text{--}1.1 \times 10^{-6}\text{ s}^{-1}$ (Yang et al., 2020). Reactivity in wildfire plumes exceeds that in urban plumes by a factor of 80–3000.

Total initial NO_3 reactivity toward BBVOCs ranges from $17.1\text{--}70.3\text{ s}^{-1}$. Reactivity of NO_3 is typically reported as a lifetime (τ_{NO_3}), which is the NO_3 concentration over the NO_3

production rate under the assumption of a steady state in both NO_3 and N_2O_5 (Brown et al., 2003). Since NO_3 and N_2O_5 readily interconvert (Reaction R4), the sum of τ_{NO_3} and $\tau_{\text{N}_2\text{O}_5}$ are reported.

$$\tau_{\text{NO}_3+\text{N}_2\text{O}_5} = \frac{\text{NO}_3 + \text{N}_2\text{O}_5}{P(\text{NO}_3)} \quad (8)$$

Using Eq. (8), modeled steady-state lifetimes are predicted to be between 0.5–1.2 s. Typical τ_{NO_3} values in urban plumes range from tens of seconds to tens of minutes, and τ_{NO_3} values in forested regions have been reported between 20 s–15 min (Brown and Stutz, 2012). The reactivity of NO_3 in wildfire plumes sampled during FIREX-AQ is $10\text{--}10^4$ times greater than typical values in forested or urban environments. The increased reactivity of NO_3 to BBVOCs within wildfire plumes is greater than the increased reactivity for OH and O_3 , highlighting that BB plumes have large overall reactivity that is more pronounced for NO_3 than other oxidants. The increased reactivity of NO_3 is due to the specific emissions from biomass burning, such as phenolics and furans that have substantial reactivity toward NO_3 . The compounds greatly increase NO_3 reactivity compared to urban VOC profiles but do not increase OH reactivity to the same degree.

In addition to a large suite of reactive BBVOCs that increase NO_3 reactivity, smoke contains concentrations of aerosol and aerosol surface area that are far greater than normally found in urban areas (Decker et al., 2019). When considering NO_3 reactivity, we must also consider aerosols, since aerosols present a loss pathway for NO_3 and its equilibrium product N_2O_5 (Brown and Stutz, 2012; Goldberger et al., 2019; Tereszchuk et al., 2011). As explained in Sect. 2.3.1, we calculate the NO_3 heterogeneous reactivity to understand the competition between NO_3 loss to BBVOCs and $\text{NO}_3/\text{N}_2\text{O}_5$ heterogeneous loss to reaction with aerosol.

As shown in Fig. S13 in the Supplement, heterogeneous losses of NO_3 and N_2O_5 are $\lesssim 2.5\%$ of total NO_3 reactivity in all model runs. Further, we find that $> 90\%$ of aerosol loss is through N_2O_5 rather than NO_3 uptake. Therefore heterogeneous losses of NO_3 and N_2O_5 do not appreciably compete with gas-phase BBVOC oxidation, consistent with a similar analysis of nighttime smoke plumes (Decker et al., 2019).

While our analysis finds that the reactivity in a BB plume is far greater than other environments, it is important to note that our calculations use a large suite of the most reactive VOCs that may not be included in other reactivity studies. Further, our reactivity calculations are based on our BBVOC ER and kinetic database as described by Decker et al., 2019. While this database includes rate coefficients for the most reactive BBVOCs, it does not include rate coefficients for all 302 BBVOCs with all oxidants. Therefore, our reactivity estimates may be a lower estimate. Our VOC profile does not include alkanes, since FIREX lab studies (Hatch et al., 2015; Koss et al., 2018) and an OH reactivity analysis of FIREX lab emissions found that OH reactivity toward alkanes accounted for 0%–1% of total BBVOC reactivity across all fuel types

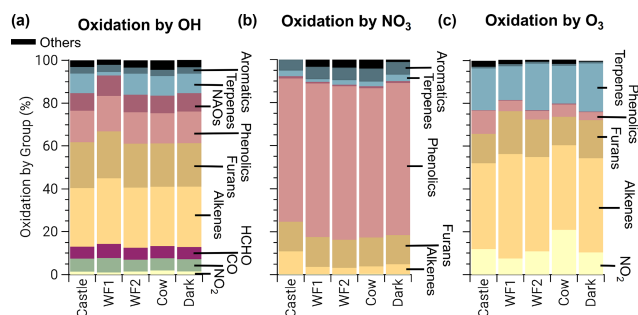


Figure 4. Integrated oxidation rate or oxidation budgets of BBVOCs by OH (a), NO_3 (b), and O_3 (c) on a relative scale for all five model runs. Oxidation by OH is spread across many BBVOC groups (where NAOs are non-aromatic oxygenates), similar to initial reactivity but also HCHO, CO, and NO_2 . Oxidation by NO_3 is dominated by phenolics but by a greater fraction than initial reactivity suggests. Oxidation by O_3 is shown without NO and is dominated by alkenes and terpenes as expected from initial reactivity, but unlike initial reactivity it includes large contributions from phenolics and NO_2 (resulting in NO_3 production).

(Gilman et al., 2015). Therefore, we expect the absent alkane reactivity in this study to be negligible.

3.2 Oxidation rates

While reactivity is a useful metric to predict the competition between reactions, it does not account for oxidant concentration, which can vary widely depending on photolysis rates, emissions, and competing oxidants. In the following sections we discuss the BBVOC oxidation rate, which is related to reactivity through the oxidant concentration as shown below

$$R_X = \sum k_{X+\text{BBVOC}_i} [\text{BBVOC}_i] [X] = k_X [X], \quad (9)$$

where R_X is the BBVOC oxidation rate; k_X is the bimolecular rate coefficient between X and BBVOC; and X is OH, NO_3 , or O_3 . In the following sections we compare and contrast reactivity and oxidation budgets and discuss how the initial reactivity changes with plume age for different BBVOC groups. Finally, we discuss the oxidant competition between NO_3 , OH, and O_3 for three main groups of BBVOCs: phenolics, furans/furfurals, and alkenes/terpenes.

3.2.1 Oxidation of BBVOCs

The integrated oxidation rate or the oxidation budget (Fig. 4) is similar to initial reactivity shown in Fig. 3 for OH oxidation, suggesting initial reactivity may be a good indicator for integrated reactivity. However, this does not hold true for NO_3 or O_3 .

The initial NO_3 reactivity differs substantially from the oxidation budget. For example, 20% of initial NO_3 reactivity is due to NO, but NO accounts for $\leq 1\%$ of integrated NO_3 loss. Further, photolysis of NO_3 accounts for $< 1\%$ of NO_3 loss in all model runs and is greatest in the Castle plume

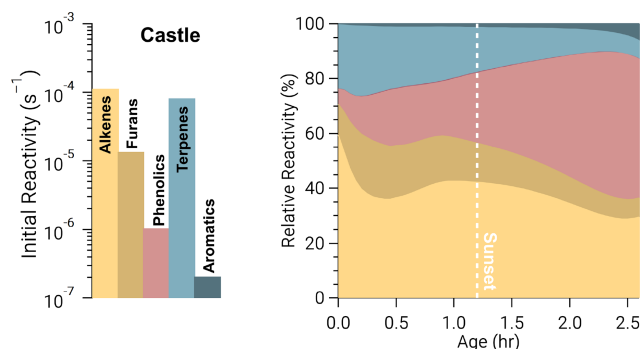


Figure 5. Ozone reactivity from the Castle model run in the form of absolute initial reactivity (bars, log scale) and relative BBVOC reactivity as a function of plume age (stacked, linear scale). As the plume ages, O_3 reactivity toward each BBVOC group changes significantly.

(0.6 %) where measured jNO_2 and calculated jNO_3 reached maximum values of 4×10^{-3} and 0.14 s^{-1} , respectively. Although daytime NO_3 oxidation of reactive VOCs has been found for heavily polluted urban air (Brown et al., 2005; Geyer et al., 2003; Osthoff et al., 2006), the dominant NO_3 loss processes in urban plumes is NO reaction and photolysis (Brown and Stutz, 2012; Wayne et al., 1991). The different controlling NO_3 loss pathway here highlights the unique and highly reactive environment of BB plumes. Further, 67%–70% of integrated NO_3 reaction is due to phenolics, which is larger than initial total NO_3 reactivity (56%). Integrated alkene, terpene, and furan oxidation by NO_3 are all lower than their initial reactivities.

The production of NO_3 , by Reaction (R3), and subsequent loss to BBVOCs is a significant (8%–21%) loss of O_3 and much greater than the initial O_3 reactivity to NO_2 of 0.4%. Similarly, integrated loss of O_3 to alkenes (40%–49%) and terpenes (16%–23%) is much less than initial reactivity would suggest (54% and 39%, respectively). Conversely, phenolics and furans account for 4%–11% and 13%–20% of O_3 loss, respectively, even though their relative initial reactivity is < 1% and 7%, respectively. Overall, the differences between initial reactivity and integrated oxidation rate are explained by changing reactivity as BBVOC are oxidized with plume age.

An example is seen in Fig. 5 for O_3 in the Castle model run, which has a large O_3 background (72 ± 1 – 82 ± 2 ppbv), is a relatively small plume, and is sunlit at emission. As a result, alkenes and terpenes are depleted quickly through oxidation by O_3 and OH. The combined O_3 reactivity of alkenes and terpenes reduces from 82% to 44% after 2 h, during which time phenolic reactivity increases from < 1% to ~ 40 %. In other words, as BBVOCs are depleted, the reactivity profile of each oxidant will change and can result in significant differences between the initial reactivity and oxidant budget.

In contrast to NO_3 and O_3 , loss of OH by each BBVOC group is within 1% of that predicted by the initial reactivity, except for terpenes. Initial reactivity of terpenes is about 13%, while actual destruction of OH by terpenes averaged to 8%. While terpene oxidation by OH is lower than its reactivity in all model runs, it is especially low (2%) in the WF1 model run, which is likely due to the large concentration of O_3 from photochemical production.

Losses of OH are not only due to highly reactive BBVOCs. HCHO, CO, and NO_2 are responsible for 12%–14% of OH destruction. This is consistent with an OH reactivity analysis from North American fuel types burned during the FIREX laboratory study, which found $13\% \pm 1\%$ of OH reactivity was due to HCHO, CO, and NO_2 (Gilman et al., 2015). The fraction of OH reactivity toward CO and NO_2 are similar to those found in a tropical rainforest (Fuchs et al., 2017) but much smaller than the fraction of OH reactivity toward CO (7%) and NO_2 (18%) found at an urban site (Gilman et al., 2009) and the fraction of OH reactivity toward CO (20%–25%) and NO_x (12%–22%) at a rural site (Edwards et al., 2013).

3.2.2 Oxidant competition

To study the competition between all oxidants, we focus on three main BBVOC groups: phenolics, furans/furfurals, and alkenes/terpenes. Generally, furans/furfurals and alkenes/terpenes groups are mainly oxidized by OH and O_3 , while NO_3 plays a small role (Fig. 6). Oxidation of furans/furfurals and alkenes/terpenes by OH (18%–55%, 11%–43%, respectively) and O_3 (39%–76%, 54%–88%, respectively) can vary widely depending on the plume. We find this is due to the variability of actinic flux. In model runs with less photolysis at emission, OH oxidation is low compared to model runs that are more optically thin. This reduction of oxidation by OH appears to be replaced by O_3 rather than NO_3 . For example, relative furan/furfural oxidation by OH in the WF1 model run (relatively large integrated jNO_2) is 31% less than that in the Cow model run (comparatively lower integrated jNO_2), yet O_3 oxidation is 32% greater.

This relationship does not hold for phenolics, which are subject to significant NO_3 oxidation (26%–52%) (Fig. 6). Phenolic oxidation by OH (22%–43%) and O_3 (16%–33%) are slightly less than NO_3 . As a result, phenolic oxidation by NO_3 dominates in the WF1 and Dark model runs, while OH dominates in the Castle model run. In the WF2 and Cow model runs, NO_3 and OH oxidation is roughly equal.

Generally, NO_3 oxidation of phenolics increases with O_3 availability and decreases with available actinic flux, but these relationships are coupled and complex. One example is seen in the WF2 model run, which has the second lowest integrated jNO_2 value, and large emissions of NO that keep O_3 low during sunlit hours. Therefore, $P(NO_3)$ is reduced, NO_3 is present at lower mixing ratios within the first hour

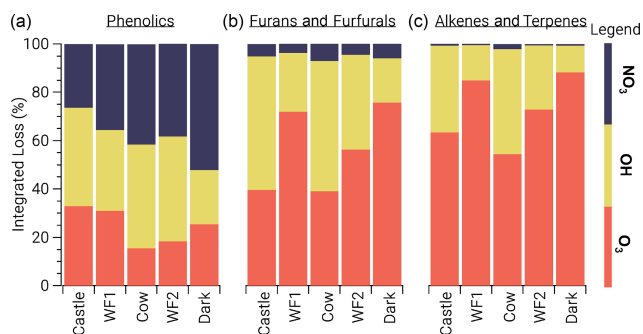


Figure 6. Integrated loss of phenolics (a), furans and furfurals (b), and alkenes and terpenes (c) reacting with NO_3 (blue), OH (yellow), and O_3 (orange). The model runs are ordered from left to right by decreasing integrated $j\text{NO}_2$. Generally, furan/furfurals and alkenes/terpenes are oxidized primarily by O_3 and OH. In contrast, phenolic oxidation is split across all oxidants.

of oxidation, and phenolics are less subject to NO_3 oxidation when compared to the other model runs.

As actinic flux increases so does OH and O_3 production, and therefore oxidant competition. One example is shown by the Castle model run where OH leads phenolic oxidation (41 %) with O_3 second (33 %). The Castle model run demonstrates the greatest observed background O_3 (90 ppbv). Further, the Castle model run has significantly smaller total emissions (based on CO) than the other model runs and the greatest integrated $j\text{NO}_2$. Due to the increased background O_3 and photochemical production of OH, NO_3 plays a smaller role in the oxidation of phenolics.

3.3 Phenolic oxidation and nitrophenolic production

The importance of phenolic oxidation for BB is evidenced by the rapidly growing literature (Bertrand et al., 2018; Chen et al., 2019; Coggon et al., 2019; Decker et al., 2019; Finewax et al., 2018; Gaston et al., 2016; Hartikainen et al., 2018; Iinuma et al., 2010; Lauraguais et al., 2014; Lin et al., 2015; Liu et al., 2019; Meng et al., 2020; Mohr et al., 2013; Palm et al., 2020; Selimovic et al., 2020; Wang and Li, 2021; Xie et al., 2017). Both OH and NO_3 oxidation of phenolics leads to nitrophenolics, which have been shown to significantly contribute to SOA production (Palm et al., 2020). However, not all nitrophenolics are created equal. Understanding the competition between phenolic oxidation by NO_3 and OH is critical, because their oxidation pathways have significantly different implications for nitrogen budgets and total nitrophenolic yield. Nitrophenolics formed by OH requires one NO_2 molecule with a nitrophenolic yield between 27 %–33 %. In contrast nitrophenolics formed by NO_3 require two molecules of NO_2 , have a yield of 85 %–97 % and produce HNO_3 as a byproduct (see Fig. S14 in the Supplement and Finewax et al., 2018).

Yet, current phenolic mechanisms are extremely limited. For example, in the MCM nitrophenolics are the only oxidation products of phenolics + NO_3 or OH, and the yields are assumed to be 100 %. Phenolic oxidation studies are typically limited to final products without detailed examination of intermediates. Phenol and cresol reactions are well studied in comparison to catechol, methylcatechol, and higher order phenolics. For that reason, we use studies of phenol and cresol oxidation to extrapolate analogous branching ratios, rate coefficients, and products for catechol, methylcatechol, and three isomers of dimethylcatechol. All of these compounds are included in the MCM, but for the purpose of the following analysis we have expanded the phenolic reaction pathways in our model as explained in the Supplement and shown in Fig. S14.

In the remaining sections, we detail how the competition for phenolic oxidation changes as the plume evolves over time. We then discuss the factors that cause differences in nitrophenolic production rate as well as how differences in OH and NO_3 phenolic oxidation lead to substantial differences in nitrocatechol yield. Finally, in the following section, we explore how nitrophenolics significantly impact the nitrogen budget.

3.3.1 Evolution of phenolic oxidation

Generally, the modeled total phenolic oxidation rate varies between 1–10 ppbv h^{-1} at emission (Fig. 7a–d), but the change in oxidation rate is not constant and trends with available actinic flux. Model runs with active initial photochemistry (Castle, WF2, and Cow) exhibit decreasing total oxidation rates, while model runs with little to no photolysis (WF1 and Dark) reach a local maximum rate after ~ 2 and ~ 5 h, respectively. These increases in oxidation rate are due to increases in O_3 and NO_3 oxidation once NO is depleted. Generally, the phenolic lifetime increases with decreasing actinic flux. The contrast between day and night phenolic oxidation is best seen by comparing the WF2 and Dark model runs. Phenolic lifetimes in the Dark model run are, on average, a factor of ~ 2 greater than phenolic lifetime in the WF2 model run.

Before sunset and in early stages of plume oxidation, the major channel of phenolic oxidation is via OH. However, in the WF1 model run NO_3 oxidation dominates after only 12 min (Fig. 7a). As the WF1 model run dilutes, photolysis rates increase and O_3 is entrained promoting O_3 and NO_3 production. This increase in oxidant concentration keeps phenolic oxidation $> 1 \text{ ppbv h}^{-1}$ for at least 4 h before the end of the model (see Sect. 2.3), unlike other model runs that drop below 1 ppbv h^{-1} of total phenolic oxidation within 0.5–3 h. After 2.6 h, in the WF1 model run, all oxidants contribute equally to phenolic oxidation; thereafter, OH and O_3 equally split oxidation, while the influence of NO_3 decreases. At the end of the WF1 model run, 69 % of initial phenolics remain unoxidized (Fig. S15 in the Supplement).

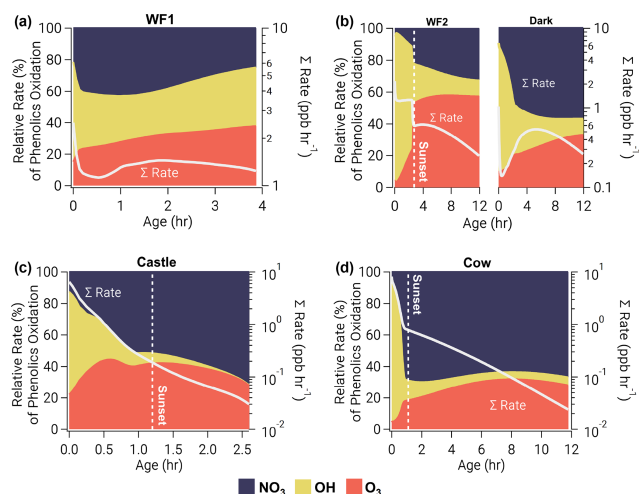


Figure 7. Relative oxidation rate (left axis) of phenolics by NO_3 (blue, top), OH (yellow, middle), and O_3 (orange, bottom) for all model runs as a function of plume age. Right axis shows absolute total reactivity (white line) on a log scale. Phenolic oxidation is controlled by OH at emission but eventually transitions to NO_3 oxidation before sunset in the WF1, Castle, and Cow model runs or after sunset in the WF2 model run. Even without photolysis, OH oxidation dominates phenolic oxidation early in the Dark model run.

As the sun sets in our sunset model runs (WF2, Castle, and Cow), a transition from OH-controlled to a mixture of NO_3 - and O_3 -controlled oxidation occurs when OH production and total oxidation rate decrease rapidly. Interestingly, OH dominates phenolic oxidation in the Dark model run (initiated after sunset) for the first 1.8 h before NO_3 oxidation takes over. During this time, OH is produced by decomposition of Criegee intermediates formed through ozonolysis of unsaturated hydrocarbons, primarily catechol (Fig. S14), methylcatechol and limonene. In other sunset model runs, OH plays a smaller role after sunset. Even so, this suggests that all BB-VOC oxidation after sunset is driven by O_3 chemistry, either through direct oxidation by O_3 , $\text{NO}_2 + \text{O}_3$ to form NO_3 , or by formation and decomposition of Criegee intermediates to form OH.

The WF2, Dark, and Cow model runs all contain unreacted phenolic emissions at sunrise the following day (48 %, 61 %, and 8 %, respectively, Fig. S15). The WF2 and Dark model runs have significantly more phenolics that remain at sunrise because of their larger (~ 3 times) emissions compared to the Cow model run. Further, the WF2 and Dark model run conditions differ only by the presence of photolysis; therefore, the difference in remaining phenolics between the WF2 and Dark is due to the time of day the smoke was emitted. In contrast to these three model runs, the emissions in Castle are depleted within 2.6 h due to its small size.

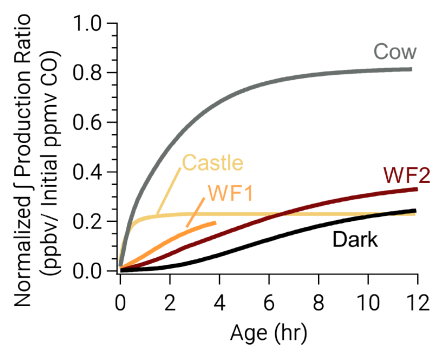


Figure 8. Integrated nitrophenolic production normalized to initial CO to compare nitrophenolic production across varying amounts of initial emissions. The simulated Castle and Cow plumes form nitrophenolics quickly. Even so, the Castle plume forms less nitrophenolics than other runs.

3.3.2 Total nitrophenolic formation

Nitrophenolic formation increases with O_3 and photolysis, which promotes formation of NO_3 and OH. For example, the Castle and Cow model runs have relatively large O_3 and $j\text{NO}_2$ at emission and therefore form nitrophenolics rapidly ($0.6\text{--}1.4\text{ ppbv h}^{-1}$ within the first 15 min). In contrast, the WF and Dark model runs have near zero O_3 due to large emissions of NO and relatively low or zero $j\text{NO}_2$ and therefore form nitrophenolics more slowly ($< 0.1\text{--}0.7\text{ ppbv h}^{-1}$ within the first 15 min).

Despite the rapid formation of nitrophenolics in the Castle model run, it has the least (excluding WF1) total nitrophenolic formation relative to total emissions as seen in Fig. 8. Figure 8 shows integrated nitrophenolic formation per emitted ppmv of CO, which allows us to compare total nitrophenolic formation across varying plume sizes. In contrast to the Castle model run, the Cow model run has the greatest nitrophenolic formation. These differences are the result of differing phenolic oxidation pathways. The Castle model run has a large (90 ppbv) O_3 background, which results in O_3 accounting for $\sim 40\%$ of phenolic oxidation between 30 min–2 h of age (Fig. 7c). At the end of the Castle model run (2.6 h), O_3 oxidation accounts for 33 % of total phenolic loss, the largest of any model run (Fig. 6). This is markedly different than the Cow model run where OH and NO_3 chemistry control phenolic oxidation before sunset and NO_3 after. While O_3 accounts for only 16 % of phenolic loss at the end of the model run (~ 12 h). In our model, the reaction of $\text{O}_3 +$ phenolics forms a ring-opening product (Fig. S14), but the rate coefficients and mechanisms are largely uncertain as discussed in the following section.

We include 157 phenolics in our above analysis, but only a few phenolics account for large fractions of nitrophenolic formation. At the end of our model runs, catechol and methylguaiacol account for the largest fraction of phenolic oxidation. Both compounds are mostly oxidized by NO_3 .

Catechol + NO₃ alone accounts for 10 %–16 % of total phenolic oxidation rate or 30 %–32 % of NO₃ + phenolic oxidation. Similarly, methylguaiacol accounts for 22 %–26 % of NO₃ + phenolic rates and is the largest fraction of phenolic oxidation by OH (17 %–18 % of OH + phenolic rates). However, to our knowledge, oxidation products of methylguaiacol by OH and NO₃ are unknown but likely lead to nitrophenolics; therefore, our nitrophenolic formation rates are likely underestimated.

3.3.3 Nitrocatechol yield

The reaction of OH and NO₃ with catechol to form nitrocatechol accounts for the largest fraction (32 %–33 %) of total nitrophenolic formation. Therefore, here, we focus on nitrocatechol and detail the nitrocatechol yield from NO₃ and OH + catechol. Understanding nitrocatechol yield and its sensitivities is important to understanding the fate of NO_x and NO_x lifetime discussed in the final sections. However, the nitrocatechol yield depends on many variables such as the concentrations of NO_x, BBVOC, O₃, and the NO_x/BBVOC ratio as well as the certainty in our chemical mechanisms. Therefore, we discuss the sensitivity of all of these factors on nitrocatechol yield below.

Yields of nitrocatechol vary between 33 %–45 % depending on the model run, where NO₃ is responsible for 72 %–92 % of nitrocatechol (Fig. 9a). Figure 9 explores factors that govern nitrocatechol yield, defined as the molar ratio of nitrocatechol production to catechol destruction. Yields of nitrocatechol from OH are low relative to NO₃ yield due to the formation of trihydroxybenzene and benzoquinones (Fig. S14), which account for 10 %–32 % and 4 %–5 % of total catechol loss, respectively.

The largest yield (45 %) is from the Dark model run, where NO₃ oxidation accounts for more than 52 % of phenolic oxidation. In contrast, the lowest yield of nitrocatechol is from the Castle model run (33 %), which has the lowest emissions of NO_x compared to the other model runs. A similar yield (34 %) is found in the WF1 model run; however, this model ends after only 4 h when 69 % of phenolics still remain. In short, nitrocatechol yield increases with increasing fraction of phenolic oxidation by NO₃.

To understand the dependence of nitrocatechol formation on O₃, NO_x, total BBVOC emissions (defined by the sum of ERs in our BBVOC inventory), and BBVOC/NO_x, we ran a sensitivity analysis on the nitrocatechol yield (Fig. 9b–e). Based on emitted NO_x and CO, BBVOC/NO_x ratios in plumes we sampled range from 11–35. However, due to fire variability, BBVOC emissions can vary by at least a factor of 2 and for many BBVOCs by more than a factor of 10 from our emission ratios (Decker et al., 2019). Furthermore, we only account for BBVOCs that are most reactive to O₃, OH, and NO₃, which is smaller than total emitted BBVOCs.

The nitrocatechol yield generally decreases with increasing BBVOC/NO_x (color scale and white lines in Fig. 9b).

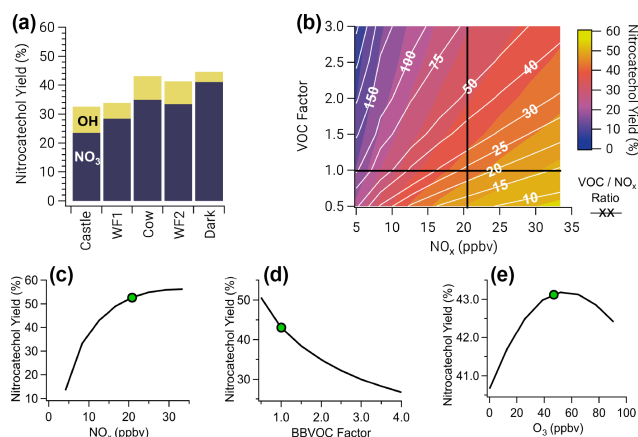


Figure 9. (a) Nitrocatechol yield for all model runs colored by the fraction of nitrocatechol formed from NO₃ and OH oxidation of catechol. Panels (b)–(e) are shown for the Cow model run, which is representative of all other runs. (b) Two overlaid contour plots of VOC/NO_x ratio (white lines and white text) and nitrocatechol yield (color scale), with black cross sections that intersect at the observed Cow conditions. (c) A cross section of (b) for nitrocatechol yield as a function of NO_x (horizontal black line). (d) A cross section of (b) for nitrocatechol yield as a function of BBVOC factor, a multiple of the initial VOC emissions (vertical black line). (e) Nitrocatechol yield as a function of initial O₃. Green dots in (c–e) indicate observed conditions used for the model run. Nitrocatechol is primarily formed from NO₃, and the yield increases with increasing NO_x but decreases with increasing BBVOC and BBVOC/NO_x ratio. Ozone has little effect on nitrocatechol yield.

As expected, nitrocatechol yields increase with increasing NO_x (Fig. 9c). Across all model runs, the nitrocatechol yield increases to 43 %–57 % over a NO_x range of 4.2–91.2 ppbv. Further, the nitrocatechol yield changes to 27 %–50 % (Fig. 9d) when varying total BBVOC emissions by a factor from 4 to 0.5. Finally, we investigate the sensitivity of nitrocatechol yield to initial O₃ and find that all model runs have little sensitivity to O₃ (Fig. 9e) with an absolute change in nitrocatechol yield < 3 % for all model runs when varying initial O₃ over a range of 0–113 ppbv.

The low sensitivity of nitrocatechol yield to O₃ may be partially explained by competition between O₃ and NO₃ + phenolic reactions after sunset. To explore this, we use a framework developed by Edwards et al. (2017). Briefly, as stated in Sect. 3.2.1, BBVOCs are the main sink for NO₃; therefore, the NO₃ loss rate is controlled by the NO₃ formation rate. As a result, NO₃ can be considered to be in approximate steady state between production by NO₂ + O₃ and loss by NO₃ + BBVOC. Further, according to Fig. 4, the majority of NO₃ is lost to phenolics. As a result, the rate of phenolic oxidation after sunset (when OH oxidation of phenolics is minimized) can be approximated as

$$-\frac{d[\text{phenolics}]}{dt} \approx (k_{\text{O}_3}[\text{phenolics}] + k_{\text{NO}_2+\text{O}_3}[\text{NO}_2][\text{O}_3]), \quad (10)$$

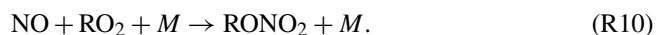
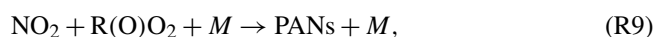
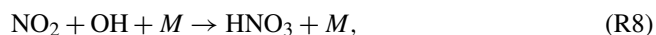
which shows that the dominant oxidant is determined by the ratio of NO_2 and phenolics. We find that the ratio of phenolics to NO_2 at which NO_3 and O_3 oxidation is equal to be ~ 10 (at 298 K, using an ER-weighted average $k_{\text{O}_3} = 2.6 \times 10^{-18} \text{ cm}^3 \text{ molecule}^{-1} \text{ s}^{-1}$) with NO_3 oxidation more important below this ratio and O_3 oxidation more important above it. Modeled phenolics/ NO_2 ratios at sunset range between 0.7–1.2, and in all model runs, except the Castle model run, the ratio decreases with age. This suggests that in all model runs NO_3 oxidation is expected to control phenolic oxidation after sunset.

The phenolic oxidation analysis above relies on phenolic mechanisms and rate coefficients that are highly uncertain. For example, the above-calculated ratio could be much lower in cold lofted plumes, but knowledge of temperature-dependent $\text{O}_3 + \text{phenolic}$ rate coefficients (k_{O_3}) are unavailable. Using temperatures observed in the WF2 plume ($\sim 268 \text{ K}$) for $k_{\text{NO}_2+\text{O}_3}$ (but using k_{O_3} at 298 K), the phenolics to NO_2 ratio at which NO_3 and O_3 oxidation is equal would be ~ 4 .

The rate coefficient and products for the reaction of catechol + O_3 that we use are generated using the MCM methodology (Jenkin et al., 2003; Saunders et al., 2003). An experimental study on the gas-phase reaction of catechol + O_3 finds an RH-dependent rate coefficient that decreases nonlinearly from 1.3×10^{-17} to $1.2 \times 10^{-19} \text{ cm}^3 \text{ molecule}^{-1} \text{ s}^{-1}$ with increasing RH (El Zein et al., 2015). The MCM uses a rate coefficient of $9.2 \times 10^{-18} \text{ cm}^3 \text{ molecule}^{-1} \text{ s}^{-1}$. Further, to our knowledge there are no experimental kinetic or mechanistic studies of phenol + O_3 . In the plumes we investigate, RH varied between roughly 20%–60%. Using an RH-dependent rate coefficient for $\text{O}_3 + \text{catechol}$, we find that the nitrocatechol yields range between 31%–58% with little change in yield for the Castle model run (–2%) and larger change for the Dark model run (+13%).

3.4 Fate of NO_x in dark BB plumes

Fire emissions are concentrated sources of NO_x , but as a result of photochemistry and oxidation the loss processes and lifetime of plume NO_x are variable. Photochemical NO_x loss pathways include reaction with OH (Reaction R8), net formation of peroxyacetyl nitrates (PANs) (Reaction R9), and formation of organic nitrates (Reaction R10).



The NO_x rate consumption is further influenced by the formation and the subsequent fate of NO_3 (Reactions R1–R4, R6–R7). Heterogeneous uptake of N_2O_5 (Reaction R5) and production of nitrophenolics double the NO_x consumption rate since in both cases subsequent chemistry consumes one additional NO_2 molecule, with the rate-limiting step being

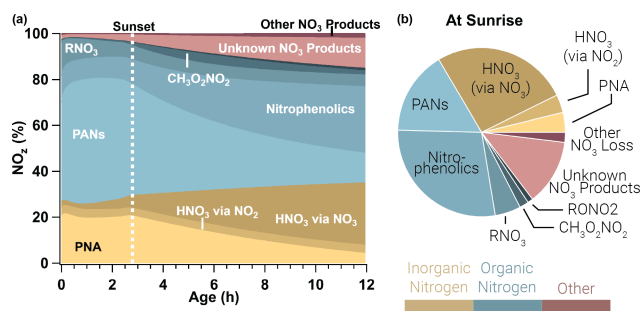


Figure 10. Relative integrated NO_x reservoirs and sinks for the WF2 model run as a function of plume age (a) and at sunrise (b). This result is the average between a WF2 model run constrained and unconstrained to peroxyacetyl nitrate observations as explained in the main text. Gold colors indicate inorganic nitrogen, blue colors indicate organic nitrogen, and red colors indicate other forms of NO_z . In this analysis we consider HONO to be a member of NO_x rather than NO_z . PANs and PNA dominate NO_z during the daytime, but after sunset these decompose to provide NO_2 that is subsequently lost to nitrophenolics and other NO_3 products overnight.

Reaction (R3). Below, we focus on the products of NO_x oxidation, determined as $\text{NO}_z = \text{NO}_y - \text{NO}_x$.

Results are similar for all model runs, and we discuss the WF2 model run as a case study. While a complete NO_z budget analysis constrained to observations is beyond the scope of this work, we compare our model results of peroxyacetyl nitrate (a component of PANs) to observations (Figs. S8 and S12). Peroxyacetyl nitrate accounts for $\sim 65\%$ of PANs, and PANs account for the largest fraction of NO_z in our model runs during sunlit hours. Our model reproduces peroxyacetyl nitrate well in one transect but underpredicts peroxyacetyl nitrate by a factor of ~ 2.5 in others. Similar to O_3 (Sect. 2.3.2), peroxyacetyl nitrate is enhanced on plume edges and the enhancement likely mixes into the center, which is not captured by our model runs. Therefore, we constrain our model to peroxyacetyl nitrate observations, present an average result (Fig. 10), and consider our model unconstrained to peroxyacetyl nitrate to be a lower-bound peroxyacetyl nitrate estimate and our model constrained to peroxyacetyl nitrate to be an upper-bound peroxyacetyl nitrate estimate.

3.4.1 NO_z budgets

The evening emitted plumes modeled in this paper exhibit photochemical loss of NO_x initially. In the period prior to sunset, PANs and PNA (peroxynitric acid, HO_2NO_2) dominate NO_z , and PANs alone account for $51\% \pm 6\%$ of NO_z by sunset. The WF2 plume is lofted and therefore cold ($\sim 267 \text{ K}$), which results in a long peroxyacetyl nitrate and PNA lifetime ($\sim 150 \text{ h}$, and $\sim 0.4 \text{ h}$, respectively, calculated from the model directly; Atkinson et al., 2006). Even so, as these plumes continue to age, PANs and PNA decompose slowly (Fig. 10) to provide NO_2 that promotes nitrophenolic for-

mation and increases nitrophenolic yield (see Sect. 3.3.3). The increase in NO_2 after sunset promotes methyl peroxy-nitrate ($\text{CH}_3\text{O}_2\text{NO}_2$) as well as NO_3 chemistry products, which grow steadily overnight. The contribution of PANs and PNA to NO_z decreases from $71\% \pm 6\%$ at sunset to $17\% \pm 2\%$ at sunrise. Relative NO_x loss to PANs and PNA is mostly replaced by the formation of nitrophenolics ($\Delta 19\% \pm 1\%$), HNO_3 by NO_3 chemistry ($\Delta 22\%$), and other or unknown NO_3 products ($\Delta 11\%$) overnight.

After sunset NO_3 chemistry takes over, and by sunrise NO_3 chemistry products lead the ($66\% \pm 2\%$) NO_z budget. Nitrophenolic formation accounts for $56\% \pm 2\%$ of NO_z in the form of HNO_3 and nitrophenolics where nitrophenolics alone account for $29\% \pm 1\%$ of NO_z ; however, most (88%) of the HNO_3 results from NO_3 chemistry. Despite accounting for only 9% (by mole) of initial emissions in our model runs, phenolics have a large and disproportionate effect on NO_x loss at night.

A similar example is seen in the Dark model run (Fig. S18 in the Supplement), where PANs and PNA dominate NO_z budget for 2.3 h until NO is depleted. At this time, PNA and PANs steadily decrease, while NO_3 products steadily increase throughout the night. By sunrise the next day, NO_3 chemistry products (including unknown products) account for 80% of NO_z . In all model runs there is a significant (12%–16%) NO_z formed through NO_3 chemistry that leads to unknown products. These unknown products are primarily the result of NO_3 + heterocycles such as furans and pyrroles, which have published rate coefficients but little mechanistic work in the literature.

Our NO_z budget generally agrees with the NO_y budget of western US wildfire smoke sampled during the 2018 Western wildfire Experiment for cloud Chemistry, Aerosol absorption and Nitrogen (WE-CAN) presented by Juncosa Calahorrano et al. (2020). Generally, the maximum fraction of PANs in our budget ($\sim 50\%$) agrees with Juncosa Calahorrano et al. ($\sim 40\%$) within our model uncertainties. Comparisons of particulate nitrate and organic nitrogen (gas or particulate) between our model run and the analysis of Juncosa Calahorrano et al. (2020) are uncertain since our model does not account for gas–particle partitioning of nitrophenolics. Our model begins to deviate from the NO_y budget trend seen by Juncosa Calahorrano et al. (2020) once the sun sets, as expected.

3.4.2 NO_x lifetime

The availability of O_3 and sunlight at emission strongly affects NO_x lifetime (τ_{NO_x} , Fig. 11) defined below

$$\tau_{\text{NO}_x} = \frac{1}{\sum_i k_i}, \quad (11)$$

where k_i is a unimolecular rate coefficient for Reactions (R3) and (R8)–(R10). Model runs with relatively large photoly-

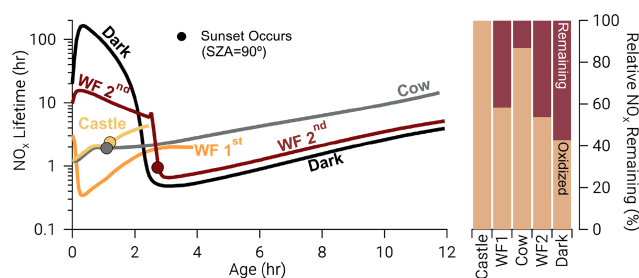


Figure 11. Time series: NO_x lifetime in hours on a log scale for all model runs where closed circles indicate the time of sunset (solar zenith angle = 90°). Bars: the relative NO_x remaining calculated as the fraction of NO_x remaining at the end of our model divided by the amount of NO_x that was reacted, excluding dilution. After the depletion of NO, NO_x chemistry changes dramatically in the WF2 and Dark model runs, reducing NO_x lifetime rapidly. A significant amount of NO_x remains in the WF2 and Dark model runs at sunrise, providing potential for significant morning chemistry to occur.

sis and O_3 at emission (Castle, Cow, and WF1) have near-emission τ_{NO_x} values that range from 1–3 h (Fig. 11), which are accompanied by larger total oxidation rates for all BBVOCs (Figs. S15–S17). These model runs also exhibit the fastest nitrophenolic formation rates (Sect. 3.3.2 and Fig. 8). In contrast model runs with low or zero photolysis and near-zero O_3 (WF2 and Dark) exhibit near-emission values of $\tau_{\text{NO}_x} \sim 10$ –16 h and $\tau_{\text{NO}_x} = 20$ –150 h, respectively. The absence of photolysis in the Dark model run explains the large difference in τ_{NO_x} between the WF2 and Dark model runs as the WF2 model run has greater O_3 and $P(\text{NO}_3)$ that promotes NO_3 chemistry as well as OH radical that promotes PANs formation. In short, we find that “daytime” conditions have shorter NO_x lifetimes, greater rates of BBVOC oxidation, and greater rates of nitrophenolic formation when compared to “nighttime” conditions.

Once NO is depleted in both model runs, NO_x chemistry changes. The BBVOC oxidation rate rapidly increases (Figs. S15–S17), and NO_x loss switches from primarily PANs and PNA to nitrophenolic production as the sun sets (Fig. 10), and O_3 is entrained from the background. As such, τ_{NO_x} decreases markedly to ~ 0.5 h.

Due to their reduced oxidation rates at emission, the WF2 and Dark model runs retain about half (46% and 57%, respectively) of the emitted NO_x by sunrise the next day. Here, we calculate remaining NO_x as the fraction of NO_x remaining at the end of our model divided by the amount of NO_x that was reacted, excluding dilution. This is about a $\Delta\text{NO}_x/\Delta\text{CO}$ ratio of ~ 4 ppbv ppmv $^{-1}$ at sunrise, which is similar to the initial emissions of Castle (~ 6 ppbv ppmv $^{-1}$) and WF1 (~ 5 ppbv ppmv $^{-1}$). Further, at sunrise, we expect the WF2 and Dark plumes to be more optically transparent and free of NO and thus oxidation rates to increase rapidly as they both still contain NO_x . An increase in oxidation at sunrise will likely be more important for the Dark model run, as

it retains 61 % of the emitted phenolics as opposed to 48 % in the WF2 model run. Plumes emitted after sunset have slower oxidation rates compared to daytime plumes (Sect. 3.2) but undergo additional oxidation from evening to morning. However, outside of the plume center, where O_3 is less effected by reaction with NO and is more likely to be generated by photochemical production, NO_x loss rates may be much larger. Therefore, NO_x away from the plume center will likely be depleted more rapidly.

4 Conclusions

This study details the competitive oxidation of BBVOCs in four near-sunset or low-photolysis smoke plumes sampled by NOAA Twin Otter or NASA DC-8 aircraft during the FIREX-AQ 2019 field campaign. We model these plumes, as well as a theoretical dark plume, using an observationally constrained 0-D chemical box model.

Our key findings and arguments are summarized below.

– Sect. 2.4: Observations and model comparison

- Our model achieves agreement with observed CO and O_3 typically within a difference of 10 %. However, strong O_3 gradients between plume center and edge can cause larger differences, specifically in the WF2 model run.
- Absolute differences between the model and observations of NO_x and HONO are generally < 1 ppbv but can be as large as 3.4 ppbv.
- In most cases, BBVOC comparisons show that the model and observations agree within a factor of ~ 2 if not within observation errors.
- Model and observation agreement for phenolics and nitrophenolics is only available for two model runs (Castle and Cow); most comparisons agree within observation errors, but some disagree by as much as a factor of 60.

– Sect. 3.1: Reactivity

- Our model suggests that OH is reactive to most BBVOCs, while NO_3 is most reactive to phenolics and O_3 to alkenes and terpenes.
- Unlike urban plumes, NO_3 loss to NO, photolysis and heterogeneous uptake are negligible loss pathways. Most (≥ 97 %) of the NO_3 loss occurs through BBVOC oxidation.
- Reactivity of OH and O_3 is similar to or greater than urban plumes, but NO_3 reactivity is a factor of 10 – 10^4 greater than typical urban plume reactivity.

– Sect. 3.2: Oxidation rates

- Initial reactivity is a good indicator for subsequent oxidation by OH but not for NO_3 and O_3 .
- Phenolics are the only BBVOC group for which oxidation by NO_3 , OH, and O_3 is competitive.
- The nitrate radical is responsible for 26 %–52 % of phenolic loss and leads (36 %) phenolic oxidation in an optically thick midday plume.

– Sect. 3.3: Phenolic oxidation and nitrophenolic production

- All phenolic oxidation after sunset is dependent on O_3 , whether through direct oxidation by O_3 , production of NO_3 by $NO_2 + O_3$, or ozonolysis of unsaturated hydrocarbons and subsequent decomposition to OH radicals.
- Yields of nitrocatechol vary between 33 %–45 %.
- Nitrate radical chemistry is responsible for 72 %–92 % (84 % in an optically thick midday plume) of nitrocatechol formation and controls nitrophenolic formation overall.

– Sect. 3.4: Fate of NO_x in dark BB plumes

- Formation of nitrophenolics by NO_3 , as opposed to OH, is the largest NO_x sink and accounts for most of the inorganic and organic nitrogen at the end of the night.
- Nitrophenolic formation pathways account for 58 %–66 % of NO_x loss by sunrise the following day.
- While both PANs and PNA account for most of the NO_x loss shortly after emission, they decompose overnight, providing a NO_x source for nitrophenolic formation, and increase nitrocatechol yield.

In short, NO_3 chemistry should be considered, even during the daytime, when investigating BB plume oxidation as we find it is the main source of nitrophenolic formation in plumes studied here and thus may be a dominant pathway to SOA formation.

Code availability. Box modeling was performed using the Framework for 0-D Atmospheric Modeling (F0AM). Details on downloading F0AM can be found at Wolfe et al. (2016; <https://github.com/AirChem/F0AM>).

Data availability. Field data used can be downloaded from <https://www-air.larc.nasa.gov/missions/firex-aq/index.html> (NASA, 2021). Emission ratio data can be found in the supplement of Decker et al. (2019).

Supplement. The supplement related to this article is available online at: <https://doi.org/10.5194/acp-21-16293-2021-supplement>.

Author contributions. FIREX-AQ data were measured and processed by the following people: UW I⁻ HR ToF CIMS (ZCJD, CDF, BBP, JAT); Tenax (KCB, PVR); Picarro G2401m (MAR, SSB); NCAR CL (FMF, DDM, GST, AJW); UHSAS (AF, AMM); jNO₂ on the Twin Otter (MAR); CO by diode laser (JPD, GSD, HH, JBW); CO by CES (JP); NOAA CL (IB, JP, TBR); ACES (SSB, MAR, JL, RAW, CW); NOAA LIF (PSR, AWR); NOAA I⁻ ToF CIMS (JAN, PRV); peroxyacetyl nitrate (LGH, YRL); UIBK PTR ToF MS (FP, AW, GIG, KS, CS, MMC); SMPS/LAS (RHM, LT, El. Wi, Ed Wi); CAFS (SH, KU); and smoke ages (CDH). Updates to the phenolic mechanism were performed by MMC, ZCJD, MAR, RHS. Model runs were conducted by ZCJD. Preparation of the article was done by ZCJD with contributions from coauthors.

Competing interests. The authors declare that they have no conflict of interest.

Disclaimer. Publisher's note: Copernicus Publications remains neutral with regard to jurisdictional claims in published maps and institutional affiliations.

Acknowledgements. Support for the UIBK PTR ToF MS came from Ionicon Analytik; Tomas Mikoviny provided technical assistance. Laura Tomsche and John Nowak supported the UIBK PTR ToF MS team as well. Thank you to Alan Fried, Dirk Richter, Jim Walega, and Petter Weibring for use of their HCHO measurements. A big thank you to all of those who helped organize and participated in the 2019 FIREX-AQ field campaign, specifically the NOAA Aircraft Operations team, including Francisco Fuenmayor, Joe Greene, Conor Maginn, Rob Miletic, Joshua Rannenberg, and David Reymore.

Financial support. Kelley C. Barsanti and Paul Van Rooy were supported by the NOAA OAR Climate Program Office (AC4 award number NA16OAR4310103). Carley D. Fredrickson, Brett B. Palm, and Joel A. Thornton were supported by the NOAA OAR Climate Program Office (award number NA17OAR4310012). The UIBK PTR-ToF-MS instrument was partly funded by the Austrian Federal Ministry for Transport, Innovation and Technology (bmvit) through the Austrian Space Applications Programme (ASAP) of the Austrian Research Promotion Agency (FFG). Felix Piel received funding from the European Union's Horizon 2020 research and innovation program under grant agreement no. 674911 (IMPACT EU ITN). Zachary Decker received funding through a graduate research award from the Cooperative Institute for Research of Environmental Sciences.

Review statement. This paper was edited by Manabu Shiraiwa and reviewed by two anonymous referees.

References

- Abatzoglou, J. T. and Williams, A. P.: Impact of anthropogenic climate change on wildfire across western US forests, *P. Natl. Acad. Sci. USA*, 113, 11770–11775, <https://doi.org/10.1073/pnas.1607171113>, 2016.
- Akagi, S. K., Yokelson, R. J., Wiedinmyer, C., Alvarado, M. J., Reid, J. S., Karl, T., Crounse, J. D., and Wennberg, P. O.: Emission factors for open and domestic biomass burning for use in atmospheric models, *Atmos. Chem. Phys.*, 11, 4039–4072, <https://doi.org/10.5194/acp-11-4039-2011>, 2011.
- Akherati, A., He, Y., Coggon, M. M., Koss, A. R., Hodshire, A. L., Sekimoto, K., Warneke, C., De Gouw, J., Yee, L., Seinfeld, J. H., Onasch, T. B., Herndon, S. C., Knighton, W. B., Cappa, C. D., Kleeman, M. J., Lim, C. Y., Kroll, J. H., Pierce, J. R., and Jathar, S. H.: Oxygenated Aromatic Compounds are Important Precursors of Secondary Organic Aerosol in Biomass-Burning Emissions, *Environ. Sci. Technol.*, 54, 8568–8579, <https://doi.org/10.1021/acs.est.0c01345>, 2020.
- Andreae, M. O. and Merlet, P.: Emissions of trace gases and aerosols from biomass burning, *Biogeochemistry*, 15, 955–966, 2001.
- Atkinson, R., Baulch, D. L., Cox, R. A., Crowley, J. N., Hampson, R. F., Hynes, R. G., Jenkin, M. E., Rossi, M. J., Troe, J., and IUPAC Subcommittee: Evaluated kinetic and photochemical data for atmospheric chemistry: Volume II—gas phase reactions of organic species, *Atmos. Chem. Phys.*, 6, 3625–4055, <https://doi.org/10.5194/acp-6-3625-2006>, 2006.
- Balch, J. K., Bradley, B. A., Abatzoglou, J. T., Chelsea Nagy, R., Fusco, E. J., and Mahood, A. L.: Human-started wildfires expand the fire niche across the United States, *P. Natl. Acad. Sci. USA*, 114, 2946–2951, <https://doi.org/10.1073/pnas.1617394114>, 2017.
- Barbero, R., Abatzoglou, J. T., Larkin, N. K., Kolden, C. A., and Stocks, B.: Climate change presents increased potential for very large fires in the contiguous United States, *Int. J. Wildland Fire*, 24, 892–899, <https://doi.org/10.1071/WF15083>, 2015.
- Bertrand, A., Stefenelli, G., Jen, C. N., Pieber, S. M., Bruns, E. A., Ni, H., Temime-Roussel, B., Slowik, J. G., Goldstein, A. H., El Haddad, I., Baltensperger, U., Prévôt, A. S. H., Wortham, H., and Marchand, N.: Evolution of the chemical fingerprint of biomass burning organic aerosol during aging, *Atmos. Chem. Phys.*, 18, 7607–7624, <https://doi.org/10.5194/acp-18-7607-2018>, 2018.
- Bishop, G. A. and Haugen, M. J.: The Story of Ever Diminishing Vehicle Tailpipe Emissions as Observed in the Chicago, Illinois Area, *Environ. Sci. Technol.*, 52, 7587–7593, <https://doi.org/10.1021/acs.est.8b00926>, 2018.
- Bloss, C., Wagner, V., Jenkin, M. E., Volkamer, R., Bloss, W. J., Lee, J. D., Heard, D. E., Wirtz, K., Martin-Reviejo, M., Rea, G., Wenger, J. C., and Pilling, M. J.: Development of a detailed chemical mechanism (MCMv3.1) for the atmospheric oxidation of aromatic hydrocarbons, *Atmos. Chem. Phys.*, 5, 641–664, <https://doi.org/10.5194/acp-5-641-2005>, 2005.
- Bolzacchini, E., Bruschi, M., Hjorth, J., Meinardi, S., Orlandi, M., Rindone, B., and Rosenbohm, E.: Gas-Phase Reaction of Phenol with NO₃, *Environ. Sci. Technol.*, 35, 1791–1797, 2001.
- Brey, S. J., Barnes, E. A., Pierce, J. R., Wiedinmyer, C., and Fischer, E. V.: Environmental Conditions, Ignition Type, and Air Quality Impacts of Wildfires in the Southeastern

- and Western United States, *Earths Future*, 6, 1442–1456, <https://doi.org/10.1029/2018EF000972>, 2018.
- Brown, S. S. and Stutz, J.: Nighttime radical observations and chemistry, *Chem. Soc. Rev.*, 41, 6405–6447, <https://doi.org/10.1039/c2cs35181a>, 2012.
- Brown, S. S., Stark, H., and Ravishankara, A. R.: Applicability of the steady state approximation to the interpretation of atmospheric observations of NO₃ and N₂O₅, *J. Geophys. Res.*, 108, 4539, <https://doi.org/10.1029/2003JD003407>, 2003.
- Brown, S. S., Osthoff, H. D., Stark, H., Dubé, W. P., Ryerson, T. B., Warneke, C., de Gouw, J. A., Wollny, A. G., Parrish, D. D., Fehsenfeld, F. C., and Ravishankara, A. R.: Aircraft observations of daytime NO₃ and N₂O₅ and their implications for tropospheric chemistry, *J. Photochem. Photobiol. A*, 176, 270–278, <https://doi.org/10.1016/j.jphotochem.2005.10.004>, 2005.
- Calvert, J. G., Mellouki, A., Orlando, J. J., Pilling, M. J., and Wallington, T. J.: *Mechanisms of Atmospheric Oxidation of the Oxygenate*, Oxford University Press, New York, 2011.
- Chang, W. L., Bhave, P. V., Brown, S. S., Riemer, N., Stutz, J., and Dabdub, D.: Heterogeneous atmospheric chemistry, ambient measurements, and model calculations of N₂O₅: A review, *Aerosol Sci. Tech.*, 45, 655–685, <https://doi.org/10.1080/02786826.2010.551672>, 2011.
- Chen, X., Sun, Y., Qi, Y., Liu, L., Xu, F., and Zhao, Y.: Mechanistic and kinetic investigations on the ozonolysis of biomass burning products: Guaiacol, syringol and creosol, *Int. J. Mol. Sci.*, 20, 4492, <https://doi.org/10.3390/ijms20184492>, 2019.
- Coggon, M. M., Lim, C. Y., Koss, A. R., Sekimoto, K., Yuan, B., Gilman, J. B., Hagan, D. H., Selimovic, V., Zarzana, K. J., Brown, S. S., Roberts, J. M., Müller, M., Yokelson, R., Wisthaler, A., Krechmer, J. E., Jimenez, J. L., Cappa, C., Kroll, J. H., de Gouw, J., and Warneke, C.: OH chemistry of non-methane organic gases (NMOGs) emitted from laboratory and ambient biomass burning smoke: evaluating the influence of furans and oxygenated aromatics on ozone and secondary NMOG formation, *Atmos. Chem. Phys.*, 19, 14875–14899, <https://doi.org/10.5194/acp-19-14875-2019>, 2019.
- Crosson, E. R.: A cavity ring-down analyzer for measuring atmospheric levels of methane, carbon dioxide, and water vapor, *Appl. Phys. B-Lasers O.*, 92, 403–408, <https://doi.org/10.1007/s00340-008-3135-y>, 2008.
- Decker, Z. C. J., Zarzana, K. J., Coggon, M., Min, K.-E., Pollack, I., Ryerson, T. B., Peischl, J., Edwards, P., Dubé, W. P., Markovic, M. Z., Roberts, J. M., Veres, P. R., Graus, M., Warneke, C., de Gouw, J., Hatch, L. E., Barsanti, K. C., and Brown, S. S.: Nighttime Chemical Transformation in Biomass Burning Plumes: A Box Model Analysis Initialized with Aircraft Observations, *Environ. Sci. Technol.*, 53, 2529–2538, <https://doi.org/10.1021/acs.est.8b05359>, 2019.
- Dennison, P. E., Brewer, S. C., Arnold, J. D., and Moritz, M. A.: Large wildfire trends in the western United States, 1984–2011, *Geophys. Res. Lett.*, 41, 2014GL059576, <https://doi.org/10.1002/2014gl059576>, 2014.
- Edwards, P. M., Evans, M. J., Furneaux, K. L., Hopkins, J., Ingham, T., Jones, C., Lee, J. D., Lewis, A. C., Moller, S. J., Stone, D., Whalley, L. K., and Heard, D. E.: OH reactivity in a South East Asian tropical rainforest during the Oxidant and Particle Photochemical Processes (OP3) project, *Atmos. Chem. Phys.*, 13, 9497–9514, <https://doi.org/10.5194/acp-13-9497-2013>, 2013.
- Edwards, P. M., Aikin, K. C., Dube, W. P., Fry, J. L., Gilman, J. B., De Gouw, J. A., Graus, M. G., Hanisco, T. F., Holloway, J., Hübler, G., Kaiser, J., Keutsch, F. N., Lerner, B. M., Neuman, J. A., Parrish, D. D., Peischl, J., Pollack, I. B., Ravishankara, A. R., Roberts, J. M., Ryerson, T. B., Trainer, M., Veres, P. R., Wolfe, G. M., and Warneke, C.: Transition from high- to low-NO_x control of night-time oxidation in the southeastern US, *Nat. Geosci.*, 10, 490–495, <https://doi.org/10.1038/ngeo2976>, 2017.
- Eilerman, S. J., Peischl, J., Neuman, J. A., Ryerson, T. B., Aikin, K. C., Holloway, M. W., Zondlo, M. A., Golston, L. M., Pan, D., Floerchinger, C., and Herndon, S.: Characterization of Ammonia, Methane, and Nitrous Oxide Emissions from Concentrated Animal Feeding Operations in North-eastern Colorado, *Environ. Sci. Technol.*, 50, 10885–10893, <https://doi.org/10.1021/acs.est.6b02851>, 2016.
- El Zein, A., Coeur, C., Obeid, E., Lauraguais, A., and Fagniez, T.: Reaction Kinetics of Catechol (1,2-Benzenediol) and Guaiacol (2-Methoxyphenol) with Ozone, *J. Phys. Chem. A*, 119, 6759–6765, <https://doi.org/10.1021/acs.jpca.5b00174>, 2015.
- Finewax, Z., De Gouw, J. A., and Ziemann, P. J.: Identification and Quantification of 4-Nitrocatechol Formed from OH and NO₃ Radical-Initiated Reactions of Catechol in Air in the Presence of NO_x: Implications for Secondary Organic Aerosol Formation from Biomass Burning, *Environ. Sci. Technol.*, 52, 1981–1989, <https://doi.org/10.1021/acs.est.7b05864>, 2018.
- Fuchs, H., Tan, Z., Lu, K., Bohn, B., Broch, S., Brown, S. S., Dong, H., Gomm, S., Häsel, R., He, L., Hofzumahaus, A., Holland, F., Li, X., Liu, Y., Lu, S., Min, K.-E., Rohrer, F., Shao, M., Wang, B., Wang, M., Wu, Y., Zeng, L., Zhang, Y., Wahner, A., and Zhang, Y.: OH reactivity at a rural site (Wangdu) in the North China Plain: contributions from OH reactants and experimental OH budget, *Atmos. Chem. Phys.*, 17, 645–661, <https://doi.org/10.5194/acp-17-645-2017>, 2017.
- Fuchs, N. A. and Sutugin, A. G.: *Highly Dispersed Aerosols*, Ann Arbor Science Publishers, Inc, Ann Arbor, 1970.
- Gaston, C. J., Lopez-Hilfiker, F. D., Whybrew, L. E., Hadley, O., McNair, F., Gao, H., Jaffe, D. A., and Thornton, J. A.: Online molecular characterization of fine particulate matter in Port Angeles, WA: Evidence for a major impact from residential wood smoke, *Atmos. Environ.*, 138, 99–107, <https://doi.org/10.1016/j.atmosenv.2016.05.013>, 2016.
- Geyer, A., Alicke, B., Ackermann, R., Martinez, M., Harder, H., Brune, W., Di Carlo, P., Williams, E., Jobson, T., Hall, S., Shetter, R., and Stutz, J.: Direct observations of daytime NO₃: Implications for urban boundary layer chemistry, *J. Geophys. Res.-Atmos.*, 108, 1–11, <https://doi.org/10.1029/2002jd002967>, 2003.
- Giglio, L.: Characterization of the tropical diurnal fire cycle using VIRS and MODIS observations, *Remote Sens. Environ.*, 108, 407–421, <https://doi.org/10.1016/j.rse.2006.11.018>, 2007.
- Gilman, J. B., Kuster, W. C., Goldan, P. D., Herndon, S. C., Zahniser, M. S., Tucker, S. C., Brewer, W. A., Lerner, B. M., Williams, E. J., Harley, R. A., Fehsenfeld, F. C., Warneke, C., and De Gouw, J. A.: Measurements of volatile organic compounds during the 2006 TexAQS/GoMACCS campaign: Industrial influences, regional characteristics, and diurnal dependencies of the OH reactivity, *J. Geophys. Res.-Atmos.*, 114, 1–17, <https://doi.org/10.1029/2008JD011525>, 2009.
- Gilman, J. B., Lerner, B. M., Kuster, W. C., Goldan, P. D., Warneke, C., Veres, P. R., Roberts, J. M., de Gouw, J. A., Burling, I.

- R., and Yokelson, R. J.: Biomass burning emissions and potential air quality impacts of volatile organic compounds and other trace gases from fuels common in the US, *Atmos. Chem. Phys.*, 15, 13915–13938, <https://doi.org/10.5194/acp-15-13915-2015>, 2015.
- Goldberger, L. A., Jahl, L. G., Thornton, J. A., and Sullivan, R. C.: N₂O₅ reactive uptake kinetics and chlorine activation on authentic biomass-burning aerosol, *Environ. Sci.-Proc. Imp.*, 21, 1684–1698, <https://doi.org/10.1039/c9em00330d>, 2019.
- Hartikainen, A., Yli-Pirilä, P., Tiitta, P., Leskinen, A., Kortelainen, M., Orasche, J., Schnelle-Kreis, J., Lehtinen, K., Zimmermann, R., Jokiniemi, J., and Sippula, O.: Volatile organic compounds from logwood combustion: Emissions and transformation under dark and photochemical aging conditions in a smog chamber, *Environ. Sci. Technol.*, 52, acs.est.7b06269, <https://doi.org/10.1021/acs.est.7b06269>, 2018.
- Hatch, L. E., Luo, W., Pankow, J. F., Yokelson, R. J., Stockwell, C. E., and Barsanti, K. C.: Identification and quantification of gaseous organic compounds emitted from biomass burning using two-dimensional gas chromatography–time-of-flight mass spectrometry, *Atmos. Chem. Phys.*, 15, 1865–1899, <https://doi.org/10.5194/acp-15-1865-2015>, 2015.
- Hatch, L. E., Yokelson, R. J., Stockwell, C. E., Veres, P. R., Simpson, I. J., Blake, D. R., Orlando, J. J., and Barsanti, K. C.: Multi-instrument comparison and compilation of non-methane organic gas emissions from biomass burning and implications for smoke-derived secondary organic aerosol precursors, *Atmos. Chem. Phys.*, 17, 1471–1489, <https://doi.org/10.5194/acp-17-1471-2017>, 2017.
- Hatch, L. E., Rivas-Ubach, A., Jen, C. N., Lipton, M., Goldstein, A. H., and Barsanti, K. C.: Measurements of I/SVOCs in biomass-burning smoke using solid-phase extraction disks and two-dimensional gas chromatography, *Atmos. Chem. Phys.*, 18, 17801–17817, <https://doi.org/10.5194/acp-18-17801-2018>, 2018.
- Higuera, P. E., Abatzoglou, J. T., Littell, J. S., and Morgan, P.: The changing strength and nature of fire-climate relationships in the northern Rocky Mountains, USA, 1902–2008, *PLoS One*, 10, 1–21, <https://doi.org/10.1371/journal.pone.0127563>, 2015.
- Holmes, C. D., Fite, C. H., Agastra, A., Schwarz, Joshua, P., Yokelson, R. J., Bui, T. P., Kondragunta, S., and Peterson, D. A.: Critical evaluation of smoke age inferred from different methods during FIREX-AQ, in: AGU Fall Meeting 2020, 16 December 2020, A225-0010, 2020.
- Iinuma, Y., Boge, O., Grade, R., and Herrmann, H.: Methyl-Nitrocatechols: Atmospheric Tracer Compounds for Biomass Burning Secondary Organic Aerosols, *Environ. Sci. Technol.*, 44, 8453–8459, 2010.
- Inciweb: 204 Cow Fire – InciWeb the Incident Information System, available at: <https://inciweb.nwcg.gov/incident/maps/6526/> (last access: 27 December 2020), 2019a.
- Inciweb: Castle Fire – InciWeb the Incident Information System, available at: <https://inciweb.nwcg.gov/incident/article/7048/53693/> (last access: 27 December 2020), 2019b.
- Inciweb: Williams Flats Fire – InciWeb the Incident Information System, available at: <https://inciweb.nwcg.gov/incident/6493/> (last access: 27 December 2020), 2019c.
- Jaffe, D. A. and Wigder, N. L.: Ozone production from wildfires: A critical review, *Atmos. Environ.*, 51, 1–10, <https://doi.org/10.1016/j.atmosenv.2011.11.063>, 2012.
- Jaffe, D. A., O'Neill, S. M., Larkin, N. K., Holder, A. L., Peterson, D. L., Halofsky, J. E., and Rappold, A. G.: Wildfire and prescribed burning impacts on air quality in the United States, *J. Air Waste Manage.*, 70, 583–615, <https://doi.org/10.1080/10962247.2020.1749731>, 2020.
- Jenkin, M. E., Saunders, S. M., and Pilling, M. J.: The tropospheric degradation of volatile organic compounds: a protocol for mechanism development, *Atmos. Environ.*, 31, 81–104, [https://doi.org/10.1016/S1352-2310\(96\)00105-7](https://doi.org/10.1016/S1352-2310(96)00105-7), 1997.
- Jenkin, M. E., Saunders, S. M., Wagner, V., and Pilling, M. J.: Protocol for the development of the Master Chemical Mechanism, MCM v3 (Part B): tropospheric degradation of aromatic volatile organic compounds, *Atmos. Chem. Phys.*, 3, 181–193, <https://doi.org/10.5194/acp-3-181-2003>, 2003.
- Jenkin, M. E., Wyche, K. P., Evans, C. J., Carr, T., Monks, P. S., Alfarra, M. R., Barley, M. H., McFiggans, G. B., Young, J. C., and Rickard, A. R.: Development and chamber evaluation of the MCM v3.2 degradation scheme for β -caryophyllene, *Atmos. Chem. Phys.*, 12, 5275–5308, <https://doi.org/10.5194/acp-12-5275-2012>, 2012.
- Jenkin, M. E., Young, J. C., and Rickard, A. R.: The MCM v3.3.1 degradation scheme for isoprene, *Atmos. Chem. Phys.*, 15, 11433–11459, <https://doi.org/10.5194/acp-15-11433-2015>, 2015.
- Juncosa Calahorrano, J. F., Lindaas, J., O'Dell, K., Palm, B. P., Peng, Q., Flocke, F., Pollack, I. B., Garofalo, L. A., Farmer, D. K., Pierce, J. R., Collett Jr, J. L., Weinheimer, A., Campos, T., Hornbrook, R. S., Hall, S. R., Ullmann, K., Pothier, M. A., Apel, E. C., Permar, W., Hu, L., Hills, A. J., Montzka, D., Tyndall, G., Thornton, J. A., and Fischer, E. V.: Day-time Oxidized Reactive Nitrogen Partitioning in Western U. S. Wildfire Smoke Plumes, *J. Geophys. Res.-Atmos.*, 126, 1–47, <https://doi.org/10.1029/2020JD033484>, 2020.
- Keywood, M., Cope, M., Meyer, C. P. P. M., Iinuma, Y., and Emmerson, K.: When smoke comes to town: The impact of biomass burning smoke on air quality, *Atmos. Environ.*, 121, 13–21, <https://doi.org/10.1016/j.atmosenv.2015.03.050>, 2015.
- Kodros, J., Papanastasiou, D., Paglione, M., Masiol, M., Squizzato, S., Florou, K., Skyllakou, K., Kaltsonoudis, C., Nenes, A., and Pandis, S. N.: The oxidizing power of the dark side: Rapid nocturnal aging of biomass burning as an overlooked source of oxidized organic aerosol, *P. Natl. Acad. Sci. USA*, 117, 33028–33033, <https://doi.org/10.1073/pnas.2010365117>, 2020.
- Kolb, C. E., Cox, R. A., Abbatt, J. P. D., Ammann, M., Davis, E. J., Donaldson, D. J., Garrett, B. C., George, C., Griffiths, P. T., Hanson, D. R., Kulmala, M., McFiggans, G., Pöschl, U., Riipinen, I., Rossi, M. J., Rudich, Y., Wagner, P. E., Winkler, P. M., Worsnop, D. R., and O'Dowd, C. D.: An overview of current issues in the uptake of atmospheric trace gases by aerosols and clouds, *Atmos. Chem. Phys.*, 10, 10561–10605, <https://doi.org/10.5194/acp-10-10561-2010>, 2010.
- Koss, A. R., Sekimoto, K., Gilman, J. B., Selimovic, V., Coggon, M. M., Zarzana, K. J., Yuan, B., Lerner, B. M., Brown, S. S., Jimenez, J. L., Krechmer, J., Roberts, J. M., Warneke, C., Yokelson, R. J., and de Gouw, J.: Non-methane organic gas emissions from biomass burning: identification, quantification,

- and emission factors from PTR-ToF during the FIREX 2016 laboratory experiment, *Atmos. Chem. Phys.*, 18, 3299–3319, <https://doi.org/10.5194/acp-18-3299-2018>, 2018.
- Kupc, A., Williamson, C., Wagner, N. L., Richardson, M., and Brock, C. A.: Modification, calibration, and performance of the Ultra-High Sensitivity Aerosol Spectrometer for particle size distribution and volatility measurements during the Atmospheric Tomography Mission (ATom) airborne campaign, *Atmos. Meas. Tech.*, 11, 369–383, <https://doi.org/10.5194/amt-11-369-2018>, 2018.
- LAS: Laser Aerosol Spectrometer 3340A, available at: <https://www.tsi.com/products/particle-sizers/particle-size-spectrometers/laser-aerosol-spectrometer-3340a/>, last access: 18 March 2021.
- Lauraguais, A., Coeur-Tourneur, C., Cassez, A., Deboudt, K., Fourmentin, M., and Choël, M.: Atmospheric reactivity of hydroxyl radicals with guaiacol (2-methoxyphenol), a biomass burning emitted compound: Secondary organic aerosol formation and gas-phase oxidation products, *Atmos. Environ.*, 86, 155–163, <https://doi.org/10.1016/j.atmosenv.2013.11.074>, 2014.
- Lee, B. H., Lopez-Hilfiker, F. D., Mohr, C., Kurtén, T., Worsnop, D. R., and Thornton, J. A.: An iodide-adduct high-resolution time-of-flight chemical-ionization mass spectrometer: Application to atmospheric inorganic and organic compounds, *Environ. Sci. Technol.*, 48, 6309–6317, <https://doi.org/10.1021/es500362a>, 2014.
- Li, F., Zhang, X., Roy, D. P., and Kondragunta, S.: Estimation of biomass-burning emissions by fusing the fire radiative power retrievals from polar-orbiting and geostationary satellites across the conterminous United States, *Atmos. Environ.*, 211, 274–287, <https://doi.org/10.1016/j.atmosenv.2019.05.017>, 2019.
- Lin, P., Liu, J., Shilling, J. E., Kathmann, S. M., Laskin, J., and Laskin, A.: Molecular characterization of brown carbon (BrC) chromophores in secondary organic aerosol generated from photo-oxidation of toluene, *Phys. Chem. Chem. Phys.*, 17, 23312–23325, <https://doi.org/10.1039/C5CP02563J>, 2015.
- Liu, C., Liu, J., Liu, Y., Chen, T., and He, H.: Secondary organic aerosol formation from the OH-initiated oxidation of guaiacol under different experimental conditions, *Atmos. Environ.*, 207, 30–37, <https://doi.org/10.1016/j.atmosenv.2019.03.021>, 2019.
- Liu, X., Zhang, Y., Huey, L. G., Yokelson, R. J., Wang, Y., Jimenez, J. L., Campuzano-Jost, P., Beyersdorf, A. J., Blake, D. R., Choi, Y., St. Clair, J. M., Crouse, J. D., Day, D. A., Diskin, G. S., Fried, A., Hall, S. R., Hanisco, T. F., King, L. E., Meinardi, S., Mikoviny, T., Palm, B. B., Peischl, J., Perring, A. E., Pollack, I. B., Ryerson, T. B., Sachse, G., Schwarz, J. P., Simpson, I. J., Tanner, D. J., Thornhill, K. L., Ullmann, K., Weber, R. J., Wennberg, P. O., Wisthaler, A., Wolfe, G. M., and Ziemba, L. D.: Agricultural fires in the southeastern U. S. during SEAC4RS: Emissions of trace gases and particles and evolution of ozone, reactive nitrogen, and organic aerosol, *J. Geophys. Res.-Atmos.*, 121, 7383–7414, <https://doi.org/10.1002/2016JD025040>, 2016.
- Lu, X., Zhang, L., Yue, X., Zhang, J., Jaffe, D. A., Stohl, A., Zhao, Y., and Shao, J.: Wildfire influences on the variability and trend of summer surface ozone in the mountainous western United States, *Atmos. Chem. Phys.*, 16, 14687–14702, <https://doi.org/10.5194/acp-16-14687-2016>, 2016.
- Marlon, J. R., Bartlein, P. J., Gavin, D. G., Long, C. J., Anderson, R. S., Briles, C. E., Brown, K. J., Colombaroli, D., Hallett, D. J., Power, M. J., Scharf, E. A., and Walsh, M. K.: Long-term perspective on wildfires in the western USA, *P. Natl. Acad. Sci. USA*, 109, 535–543, <https://doi.org/10.1073/pnas.1112839109>, 2012.
- McDuffie, E. E., Fibiger, D. L., Dubé, W. P., Lopez-Hilfiker, F., Lee, B. H., Thornton, J. A., Shah, V., Jaeglé, L., Guo, H., Weber, R. J., Michael Reeves, J., Weinheimer, A. J., Schroder, J. C., Campuzano-Jost, P., Jimenez, J. L., Dibb, J. E., Veres, P., Ebben, C., Sparks, T. L., Wooldridge, P. J., Cohen, R. C., Hornbrook, R. S., Apel, E. C., Campos, T., Hall, S. R., Ullmann, K., and Brown, S. S.: Heterogeneous N₂O₅ Uptake During Winter: Aircraft Measurements During the 2015 WINTER Campaign and Critical Evaluation of Current Parameterizations, *J. Geophys. Res.-Atmos.*, 123, 4345–4372, <https://doi.org/10.1002/2018JD028336>, 2018.
- Meng, L., Coeur, C., Fayad, L., Houzel, N., Genevray, P., Bouzidi, H., Tomas, A., and Chen, W.: Secondary organic aerosol formation from the gas-phase reaction of guaiacol (2-methoxyphenol) with NO₃ radicals, *Atmos. Environ.*, 240, 117740, <https://doi.org/10.1016/j.atmosenv.2020.117740>, 2020.
- Min, K.-E., Washenfelder, R. A., Dubé, W. P., Langford, A. O., Edwards, P. M., Zarzana, K. J., Stutz, J., Lu, K., Rohrer, F., Zhang, Y., and Brown, S. S.: A broadband cavity enhanced absorption spectrometer for aircraft measurements of glyoxal, methylglyoxal, nitrous acid, nitrogen dioxide, and water vapor, *Atmos. Meas. Tech.*, 9, 423–440, <https://doi.org/10.5194/amt-9-423-2016>, 2016.
- Mohr, C., Lopez-Hilfiker, F. D., Zotter, P., Prévôt, A. S. H., Xu, L., Ng, N. L., Herndon, S. C., Williams, L. R., Franklin, J. P., Zahniser, M. S., Worsnop, D. R., Knighton, W. B., Aiken, A. C., Gorkowski, K. J., Dubey, M. K., Allan, J. D., and Thornton, J. A.: Contribution of Nitrated Phenols to Wood Burning Brown Carbon Light Absorption in Detling, United Kingdom During Winter Time, *Environ. Sci. Technol.*, 47, 6316–6324, <https://doi.org/10.1021/es400683v>, 2013.
- Mondello, L., Tranchida, P. Q., Dugo, P., and Dugo, G.: Comprehensive two-dimensional gas chromatography-mass spectrometry: A review, *Mass Spectrom. Rev.*, 27, 101–124, <https://doi.org/10.1002/mas.20158>, 2008.
- Moore, R. H., Wiggins, E. B., Ahern, A. T., Zimmerman, S., Montgomery, L., Campuzano Jost, P., Robinson, C. E., Ziemba, L. D., Winstead, E. L., Anderson, B. E., Brock, C. A., Brown, M. D., Chen, G., Crosbie, E. C., Guo, H., Jimenez, J. L., Jordan, C. E., Lyu, M., Nault, B. A., Rothfuss, N. E., Sanchez, K. J., Schueneman, M., Shingler, T. J., Shook, M. A., Thornhill, K. L., Wagner, N. L., and Wang, J.: Sizing response of the Ultra-High Sensitivity Aerosol Spectrometer (UHSAS) and Laser Aerosol Spectrometer (LAS) to changes in submicron aerosol composition and refractive index, *Atmos. Meas. Tech.*, 14, 4517–4542, <https://doi.org/10.5194/amt-14-4517-2021>, 2021.
- Müller, M., Mikoviny, T., Feil, S., Haidacher, S., Hanel, G., Hartungen, E., Jordan, A., Märk, L., Mutschlechner, P., Schottkowsky, R., Sulzer, P., Crawford, J. H., and Wisthaler, A.: A compact PTR-ToF-MS instrument for airborne measurements of volatile organic compounds at high spatiotemporal resolution, *Atmos. Meas. Tech.*, 7, 3763–3772, <https://doi.org/10.5194/amt-7-3763-2014>, 2014.
- Nakao, S., Clark, C., Tang, P., Sato, K., and Cocker III, D.: Secondary organic aerosol formation from phenolic compounds in

- the absence of NO_x, *Atmos. Chem. Phys.*, 11, 10649–10660, <https://doi.org/10.5194/acp-11-10649-2011>, 2011.
- NASA: FIREX-AQ, NASA [data set], available at: <https://www-air.larc.nasa.gov/missions/firex-aq/index.html>, last access: 24 October 2021.
- Neuman, J. A., Trainer, M., Brown, S. S., Min, K. E., Nowak, J. B., Parrish, D. D., Peischl, J., Pollack, I. B., Roberts, J. M., Ryerson, T. B., and Veres, P. R.: HONO emission and production determined from airborne measurements over the Southeast U. S., *J. Geophys. Res.*, 121, 9237–9250, <https://doi.org/10.1002/2016JD025197>, 2016.
- NIFC: NIFC 2019 Statistics and Summary, available at: https://www.predictiveservices.nifc.gov/intelligence/2019_statsum/2019Stats&Summ.html (last access: 8 January 2021), 2019.
- Olariu, R., Klotz, B., Barnes, I., Becker, K., and Mocanu, R.: FT-IR study of the ring-retaining products from the reaction of OH radicals with phenol, o-, m-, and p-cresol, *Atmos. Environ.*, 36, 3685–3697, [https://doi.org/10.1016/S1352-2310\(02\)00202-9](https://doi.org/10.1016/S1352-2310(02)00202-9), 2002.
- Olariu, R. I., Barnes, I., Bejan, I., Arsene, C., Vione, D., Klotz, B., and Becker, K. H.: FT-IR Product Study of the Reactions of NO₃ Radicals With ortho-, meta-, and para-Cresol, *Environ. Sci. Technol.*, 47, 7729–7738, <https://doi.org/10.1021/es401096w>, 2013.
- Osthoff, H. D., Sommariva, R., Baynard, T., Pettersson, A., Williams, E. J., Lerner, B. M., Roberts, J. M., Stark, H., Goldan, P. D., Kuster, W. C., Bates, T. S., Coffman, D., Ravishankara, A. R., and Brown, S. S.: Observation of daytime N₂O₅ in the marine boundary layer during New England Air Quality Study – Intercontinental Transport and Chemical Transformation 2004, *J. Geophys. Res.-Atmos.*, 111, D23S14, <https://doi.org/10.1029/2006JD007593>, 2006.
- Palm, B. B., Campuzano-Jost, P., Day, D. A., Ortega, A. M., Fry, J. L., Brown, S. S., Zarzana, K. J., Dube, W., Wagner, N. L., Draper, D. C., Kaser, L., Jud, W., Karl, T., Hansel, A., Gutiérrez-Montes, C., and Jimenez, J. L.: Secondary organic aerosol formation from in situ OH, O₃, and NO₃ oxidation of ambient forest air in an oxidation flow reactor, *Atmos. Chem. Phys.*, 17, 5331–5354, <https://doi.org/10.5194/acp-17-5331-2017>, 2017.
- Palm, B. B., Peng, Q., Fredrickson, C. D., Lee, B. H., Garofalo, L. A., Pothier, M. A., Kreidenweis, S. M., Farmer, D. K., Pokhrel, R. P., Shen, Y., Murphy, S. M., Permar, W., Hu, L., Campos, T. L., Hall, S. R., Ullmann, K., Zhang, X., Flocke, F., Fischer, E. V., and Thornton, J. A.: Quantification of organic aerosol and brown carbon evolution in fresh wildfire plumes, *P. Natl. Acad. Sci. USA*, 117, 29469–29477, <https://doi.org/10.1073/pnas.2012218117>, 2020.
- Parks, S. A., Miller, C., Parisien, M. A., Holsinger, L. M., Dobrowski, S. Z., and Abatzoglou, J.: Wildland fire deficit and surplus in the western United States, 1984–2012, *Ecosphere*, 6, 1–13, <https://doi.org/10.1890/ES15-00294.1>, 2015.
- Peng, Q., Palm, B. B., Melander, K. E., Lee, B. H., Hall, S. R., Ullmann, K., Campos, T., Weinheimer, A. J., Apel, E. C., Hornbrook, R. S., Hills, A. J., Montzka, D. D., Flocke, F., Hu, L., Permar, W., Wielgasz, C., Lindaas, J., Pollack, I. B., Fischer, E. V., Bertram, T. H., and Thornton, J. A.: HONO Emissions from Western U. S. Wildfires Provide Dominant Radical Source in Fresh Wildfire Smoke, *Environ. Sci. Technol.*, 54, 5954–5963, <https://doi.org/10.1021/acs.est.0c00126>, 2020.
- Phuleria, H. C., Fine, P. M., Zhu, Y., and Sioutas, C.: Air quality impacts of the October 2003 Southern California wildfires, *J. Geophys. Res.-Atmos.*, 110, 1–11, <https://doi.org/10.1029/2004JD004626>, 2005.
- Pollack, I. B., Lerner, B. M., and Ryerson, T. B.: Evaluation of ultraviolet light-emitting diodes for detection of atmospheric NO₂ by photolysis – Chemiluminescence, *J. Atmos. Chem.*, 65, 111–125, <https://doi.org/10.1007/s10874-011-9184-3>, 2010.
- Ridley, B. A., Grahek, F. E., and Walega, J. G.: A Small High-Sensitivity, Medium-Response Ozone Detector Suitable for Measurements from Light Aircraft, *J. Atmos. Ocean. Tech.*, 9, 142–148, [https://doi.org/10.1175/1520-0426\(1992\)009<0142:ASHSMR>2.0.CO;2](https://doi.org/10.1175/1520-0426(1992)009<0142:ASHSMR>2.0.CO;2), 1992.
- Ro Lee, Y., Ji, Y., Tanner, D. J., and Huey, L. G.: A low-activity ion source for measurement of atmospheric gases by chemical ionization mass spectrometry, *Atmos. Meas. Tech.*, 13, 2473–2480, <https://doi.org/10.5194/amt-13-2473-2020>, 2020.
- Roberts, J. M., Stockwell, C. E., Yokelson, R. J., de Gouw, J., Liu, Y., Selimovic, V., Koss, A. R., Sekimoto, K., Coggon, M. M., Yuan, B., Zarzana, K. J., Brown, S. S., Santin, C., Doerr, S. H., and Warneke, C.: The nitrogen budget of laboratory-simulated western US wildfires during the FIREX 2016 Fire Lab study, *Atmos. Chem. Phys.*, 20, 8807–8826, <https://doi.org/10.5194/acp-20-8807-2020>, 2020.
- Robinson, M. A., Decker, Z. C. J., Barsanti, K. C., Coggon, M. M., Flocke, F. M., Franchin, A., Fredrickson, C. D., Gilman, J. B., Gkatzelis, G. I., Holmes, C. D., Lamplugh, A., Lavi, A., Middlebrook, A. M., Montzka, D. M., Palm, B. B., Peischl, J., Pierce, B., Schwantes, R. H., Sekimoto, K., Selimovic, V., Tyndall, G. S., Thornton, J. A., Rooy, P. Van, Warneke, C., Weinheimer, A. J., and Brown, S. S.: Variability and Time of Day Dependence of Ozone Photochemistry in Western Wildfire Plumes, *Environ. Sci. Technol.*, 55, 10280–10290, <https://doi.org/10.1021/ACS.EST.1C01963>, 2021.
- Rollins, A. W., Rickly, P. S., Gao, R.-S., Ryerson, T. B., Brown, S. S., Peischl, J., and Bourgeois, I.: Single-photon laser-induced fluorescence detection of nitric oxide at sub-parts-per-trillion mixing ratios, *Atmos. Meas. Tech.*, 13, 2425–2439, <https://doi.org/10.5194/amt-13-2425-2020>, 2020.
- Sachse, G. W., Collins Jr, J. E., Hill, G. F., Wade, L. O., Lewis, B. G., and Ritter, J. A.: Airborne tunable diode laser sensor for high-precision concentration and flux measurements of carbon monoxide and methane, *Proc. SPIE*, 1433, 157–166, <https://doi.org/10.1117/12.46162>, 1991.
- Sangwan, M. and Zhu, L.: Absorption cross sections of 2-Nitrophenol in the 295–400 nm region and photolysis of 2-Nitrophenol at 308 and 351 nm, *J. Phys. Chem. A*, 120, 9958–9967, <https://doi.org/10.1021/acs.jpca.6b08961>, 2016.
- Sangwan, M. and Zhu, L.: Role of Methyl-2-nitrophenol Photolysis as a Potential Source of OH Radicals in the Polluted Atmosphere: Implications from Laboratory Investigation, *J. Phys. Chem. A*, 122, 1861–1872, <https://doi.org/10.1021/acs.jpca.7b11235>, 2018.
- Saunders, S. M., Pascoe, S., Johnson, A. P., Pilling, M. J., and Jenkin, M. E.: Development and preliminary test results of an expert system for the automatic generation of tropospheric VOC degradation mechanisms, *Atmos. Environ.*, 37, 1723–1735, [https://doi.org/10.1016/S1352-2310\(03\)00072-4](https://doi.org/10.1016/S1352-2310(03)00072-4), 2003.

- Schwantes, R. H., Schilling, K. A., McVay, R. C., Lignell, H., Coggon, M. M., Zhang, X., Wennberg, P. O., and Seinfeld, J. H.: Formation of highly oxygenated low-volatility products from cresol oxidation, *Atmos. Chem. Phys.*, 17, 3453–3474, <https://doi.org/10.5194/acp-17-3453-2017>, 2017.
- Selimovic, V., Yokelson, R. J., McMeeking, G. R., and Coefield, S.: Aerosol Mass and Optical Properties, Smoke Influence on O₃, and High NO₃ Production Rates in a Western U. S. City Impacted by Wildfires, *J. Geophys. Res.-Atmos.*, 125, 1–22, <https://doi.org/10.1029/2020JD032791>, 2020.
- Shetter, R. E. and Müller, M.: Photolysis frequency measurements using actinic flux spectroradiometry during the PEM-Tropics mission: Instrumentation description and some results, *J. Geophys. Res.-Atmos.*, 104, 5647–5661, <https://doi.org/10.1029/98JD01381>, 1999.
- Silvern, R. F., Jacob, D. J., Mickley, L. J., Sulprizio, M. P., Travis, K. R., Marais, E. A., Cohen, R. C., Laughner, J. L., Choi, S., Joiner, J., and Lamsal, L. N.: Using satellite observations of tropospheric NO₂ columns to infer long-term trends in US NO_x emissions: the importance of accounting for the free tropospheric NO₂ background, *Atmos. Chem. Phys.*, 19, 8863–8878, <https://doi.org/10.5194/acp-19-8863-2019>, 2019.
- SMPS: Scanning Mobility Particle Sizer Spectrometer 3936, available at: <https://tsi.com/discontinued-products/scanning-mobility-particle-sizer-spectrometer-3936/>, last access: 18 March 2021.
- Sparks, T. L., Ebben, C. J., Wooldridge, P. J., Lopez-Hilfiker, F. D., Lee, B. H., Thornton, J. A., McDuffie, E. E., Fibiger, D. L., Brown, S. S., Montzka, D. D., Weinheimer, A. J., Schroder, J. C., Campuzano-Jost, P., Jimenez, J. L., and Cohen, R. C.: Comparison of Airborne Reactive Nitrogen Measurements During WINTER, *J. Geophys. Res.-Atmos.*, 124, 10483–10502, <https://doi.org/10.1029/2019JD030700>, 2019.
- Stedman, D. H., Daby, E. E., Stuhl, F., and Niki, H.: Analysis of ozone and nitric oxide by a chemiluminescent method in laboratory and atmospheric studies of photochemical smog, *JAPCA J. Air Waste Ma.*, 22, 260–263, <https://doi.org/10.1080/00022470.1972.10469635>, 1972.
- Tereszczuk, K. A., González Abad, G., Clerbaux, C., Hurtmans, D., Coheur, P.-F., and Bernath, P. F.: ACE-FTS measurements of trace species in the characterization of biomass burning plumes, *Atmos. Chem. Phys.*, 11, 12169–12179, <https://doi.org/10.5194/acp-11-12169-2011>, 2011.
- Veres, P. R., Andrew Neuman, J., Bertram, T. H., Assaf, E., Wolfe, G. M., Williamson, C. J., Weinzierl, B., Tilmes, S., Thompson, C. R., Thames, A. B., Schroder, J. C., Saiz-Lopez, A., Rollins, A. W., Roberts, J. M., Price, D., Peischl, J., Nault, B. A., Møller, K. H., Miller, D. O., Meinardi, S., Li, Q., Lamarque, J. F., Kupc, A., Kjaergaard, H. G., Kinnison, D., Jimenez, J. L., Jernigan, C. M., Hornbrook, R. S., Hills, A., Dollner, M., Day, D. A., Cuevas, C. A., Campuzano-Jost, P., Burkholder, J., Paul Bui, T., Brune, W. H., Brown, S. S., Brock, C. A., Bourgeois, I., Blake, D. R., Apel, E. C., and Ryerson, T. B.: Global airborne sampling reveals a previously unobserved dimethyl sulfide oxidation mechanism in the marine atmosphere, *P. Natl. Acad. Sci. USA*, 117, 4505–4510, <https://doi.org/10.1073/pnas.1919344117>, 2020.
- Wagner, N. L., Riedel, T. P., Young, C. J., Bahreini, R., Brock, C. A., Dubé, W. P., Kim, S., Middlebrook, A. M., Öztürk, F., Roberts, J. M., Russo, R., Sive, B., Swarthout, R., Thornton, J. A., Vandenberg, T. C., Zhou, Y., and Brown, S. S.: N₂O₅ uptake coefficients and nocturnal NO₂ removal rates determined from ambient wintertime measurements, *J. Geophys. Res.-Atmos.*, 118, 9331–9350, <https://doi.org/10.1002/jgrd.50653>, 2013.
- Wang, S. and Li, H.: NO₃[•]-Initiated Gas-Phase Formation of Nitrated Phenolic Compounds in Polluted Atmosphere, *Environ. Sci. Technol.*, 55, 2899–2907, <https://doi.org/10.1021/acs.est.0c08041>, 2021.
- Warneke, C., De Gouw, J. A., Holloway, J. S., Peischl, J., Ryerson, T. B., Atlas, E., Blake, D., Trainer, M., and Parrish, D. D.: Multiyear trends in volatile organic compounds in Los Angeles, California: Five decades of decreasing emissions, *J. Geophys. Res.-Atmos.*, 117, 1–10, <https://doi.org/10.1029/2012JD017899>, 2012.
- Warneke, C., Trainer, M., de Gouw, J. A., Parrish, D. D., Fahey, D. W., Ravishankara, A. R., Middlebrook, A. M., Brock, C. A., Roberts, J. M., Brown, S. S., Neuman, J. A., Lerner, B. M., Lack, D., Law, D., Hübler, G., Pollack, I., Sjostedt, S., Ryerson, T. B., Gilman, J. B., Liao, J., Holloway, J., Peischl, J., Nowak, J. B., Aikin, K. C., Min, K.-E., Washenfelder, R. A., Graus, M. G., Richardson, M., Markovic, M. Z., Wagner, N. L., Welti, A., Veres, P. R., Edwards, P., Schwarz, J. P., Gordon, T., Dube, W. P., McKeen, S. A., Brioude, J., Ahmadov, R., Bougiatioti, A., Lin, J. J., Nenes, A., Wolfe, G. M., Hanisco, T. F., Lee, B. H., Lopez-Hilfiker, F. D., Thornton, J. A., Keutsch, F. N., Kaiser, J., Mao, J., and Hatcher, C. D.: Instrumentation and measurement strategy for the NOAA SENEX aircraft campaign as part of the Southeast Atmosphere Study 2013, *Atmos. Meas. Tech.*, 9, 3063–3093, <https://doi.org/10.5194/amt-9-3063-2016>, 2016.
- Wayne, R. P., Barnes, I., Biggs, P., Burrows, J. P., Canosa-Mas, C. E., Hjorth, J., Le Bras, G., Moortgat, G. K., Perner, D., Poulet, G., Restelli, G., and Sidebottom, H.: The nitrate radical: Physics, chemistry, and the atmosphere, *Atmos. Environ. A-Gen.*, 25, 1–203, [https://doi.org/10.1016/0960-1686\(91\)90192-A](https://doi.org/10.1016/0960-1686(91)90192-A), 1991.
- Westerling, A. L., Hidalgo, H. G., Cayan, D. R., and Swetnam, T. W.: Warming and Earlier Spring Increase Western U. S. Forest Wildfire Activity, *Science*, 313, 940–943, 2006.
- Westerling, A. L. R.: Increasing western US forest wildfire activity: Sensitivity to changes in the timing of spring, *Philos. T. R. Soc. B*, 371, <https://doi.org/10.1098/rstb.2015.0178>, 2016.
- Williams, A. P., Abatzoglou, J. T., Gershunov, A., Guzman-Morales, J., Bishop, D. A., Balch, J. K., and Lettenmaier, D. P.: Observed Impacts of Anthropogenic Climate Change on Wildfire in California, *Earths Future*, 7, 892–910, <https://doi.org/10.1029/2019EF001210>, 2019.
- Wolfe, G. M., Marvin, M. R., Roberts, S. J., Travis, K. R., and Liao, J.: The Framework for 0-D Atmospheric Modeling (FOAM) v3.1, *Geosci. Model Dev.*, 9, 3309–3319, <https://doi.org/10.5194/gmd-9-3309-2016>, 2016 (code available at: <https://github.com/AirChem/FOAM>, last access: 26 October 2021).
- Xie, M., Chen, X., Hays, M. D., Lewandowski, M., Offenberg, J., Kleindienst, T. E., and Holder, A. L.: Light Absorption of Secondary Organic Aerosol: Composition and Contribution of Nitroaromatic Compounds, *Environ. Sci. Technol.*, 51, 11607–11616, <https://doi.org/10.1021/acs.est.7b03263>, 2017.
- Xing, J., Mathur, R., Pleim, J., Hogrefe, C., Gan, C.-M., Wong, D. C., Wei, C., Gilliam, R., and Pouliot, G.: Observations and modeling of air quality trends over 1990–2010 across the North-

- ern Hemisphere: China, the United States and Europe, *Atmos. Chem. Phys.*, 15, 2723–2747, <https://doi.org/10.5194/acp-15-2723-2015>, 2015.
- Yang, Y., Shao, M., Wang, X., Nölscher, A. C., Kessel, S., Guenther, A., and Williams, J.: Towards a quantitative understanding of total OH reactivity: A review, *Atmos. Environ.*, 134, 147–161, <https://doi.org/10.1016/j.atmosenv.2016.03.010>, 2016.
- Yang, Y., Wang, Y., Zhou, P., Yao, D., Ji, D., Sun, J., Wang, Y., Zhao, S., Huang, W., Yang, S., Chen, D., Gao, W., Liu, Z., Hu, B., Zhang, R., Zeng, L., Ge, M., Petäjä, T., Kerminen, V.-M., Kulmala, M., and Wang, Y.: Atmospheric reactivity and oxidation capacity during summer at a suburban site between Beijing and Tianjin, *Atmos. Chem. Phys.*, 20, 8181–8200, <https://doi.org/10.5194/acp-20-8181-2020>, 2020.
- Yokelson, R. J., Andreae, M. O., and Akagi, S. K.: Pitfalls with the use of enhancement ratios or normalized excess mixing ratios measured in plumes to characterize pollution sources and aging, *Atmos. Meas. Tech.*, 6, 2155–2158, <https://doi.org/10.5194/amt-6-2155-2013>, 2013.